TOTAL INTERNAL REFLECTION HOLOGRAPHIC MICROSCOPY FOR CELL EXTENSION IMAGING

by

Tolga Gürcan

B.S., Physics, Boğaziçi University, 2020

Submitted to the Institute for Graduate Studies in
Science and Engineering in partial fulfillment of
the requirements for the degree of
Master of Science

Graduate Program in Physics
Boğaziçi University
2022

ACKNOWLEDGEMENTS

I sincerely would like to thank my thesis advisors Prof. Mehmet Burçin Ünlü and Assist. Prof. Muhammed Fatih Toy, for their support, encouragement, and guidance throughout my M.Sc. thesis. Without their motivation and enthusiasm, it would not have been possible to write the thesis. Their advice on personal and professional matters made me a better version of myself.

I would like to thank all the former and present group members of BUMILAB, especially Uğur Parlatan, Nasire Uluç, Seydi Yavaş, and Gizem Alpakut, not only for sharing their abundant knowledge, beneficial scientific discussions and for being helpful to me but also for being great friends outside of the lab too.

I would especially like to thank Berker Gönül and Ahmet Gezici for their long-standing friendship, invaluable support, and being a source of joy in my life.

I would also like to thank my thesis committee members for sparing their valuable time and for their reviews and corrections on my thesis.

The Financial support during my studies from TÜBİTAK (Project no: 120F099) is also gratefully acknowledged.

Son olarak şimdiye kadar bana olan desteklerini hiç esirgemeyen, aldığım her kararda yanımda olan aileme, Habibe ve Şaban Gürcan'a sonsuz teşekkürlerimi sunuyorum.

ABSTRACT

TOTAL INTERNAL REFLECTION HOLOGRAPHIC MICROSCOPY FOR CELL EXTENSION IMAGING

The study of interfacial structures is of utmost importance not only for various research fields such as cell biology and display systems but also their sub-disciplines. One of the traditional means of imaging buried structures rely on fluorescence labeling and the use of optical sectioning with superresolution microscopy. Although it exceeds diffraction limit, there are various shortcomings to utilize this methodology such as its reliance on fluorescent markers, long exposure times to high cost of the imaging system. Ultimately, these limitations position the existing technologies unideal for live cell imaging, including the imaging of surface proteins of a living cell. A label free quantitative phase imaging method is realized in this study to enable imaging of an interface between different media. This system is based on off-axis holographic microscopy and uses a high numerical aperture (NA) microscope objective to achieve total internal reflection (TIR). Existing literature on total internal reflection holographic microscopy utilizes prism to achieve TIR which limits the working distance of objective to be large hence resolution. Proposed system relies on a 100x objective with 1.49 NA to improve resolution and magnification. Complex field which is reflected from burried interface of the sample can be recovered by using digital holography principles. The resolution of the system can further be enhanced by combining several illumination angles and utilizing synthetic aperture reconstruction. Also a new iterative algorithm for maskless grayscale lithography which uses quantitative phase measurements as feedback is realized in this study. Phase measurements are performed via an off-axis digital holography configuration. A spiral phase plate which has uses in superresolution microscopy techniques is produced with proposed algorithm and shown to perform better compared to classical method.

ÖZET

HOLOGRAFİK TAM İÇ YANSIMA MİKROSKOBUYLA HÜCRE UZANTILARININ GÖRÜNTÜLENMESİ

Arayüz yapılarının incelenmesi biyoloji, ekran sistemleri gibi bir çok alan ve alt alanları için büyük öneme sahiptir. Klasik olarak bu yapıların incelenmesi floresan boyayla işaretlendikten sonra optik kesitleme, süperçözünürlük görüntüleme sistemleri ile birleştirilerek yapılmaktadır. Bu yöntemlerle kırınım limitini aşan çözünürlüklere ulaşılabilmesine rağmen floresan görüntüleme için gereken uzun pozlama süreleri, yüksek maliyet gibi bir çok sıkıntıyı beraberinde getirirler. Bu kısıtlamalar var olan yöntemleri canlı hücre görüntüleme uygulamaları için elverişsiz kılmaktadır. Bu projede hücre ve bulunduğu ortam arasındaki bir işaretlemeye gerek kalmadan incelemeyi sağlayacak bir nicel faz görüntüleme sistemi gerçekleştirilmiştir. Eksen dışı bir holografik mikroskop temelli olan sistem, tam iç yansımayı yüksek numerik açıklıklı bir objektif kullanarak oluşturacaktır. Literatürde var olan çalışmalarda tam iç yansıma, bir prizma kullanılarak gerçekleştirilmektedir. Fakat prizmanın fiziksel boyutları, kullanılacak objektifin numerik açıklığını ve sistemin büyütmesini sınırlamaktadır. Burada geliştirilen sistemde 1.49 numerik açıklığa sahip 100x bir objektif kullanılarak hücre arayüzünde bulunan yapıların görüntülemesi yapılacaktır. Örnekten yansıyan kompleks dalga dijital holografi prensipleri kullanılarak geri oluşturulacaktır. Sistemin çözünürlüğü birden fazla aydınlatma açısından elde edilen kompleks alanların birleştirilmesi ile kırınım limitinin üstüne çıkabilecektir. Bunlara ek olarak microoptik malzemelerin üretilmesine olanak sağlayan yeni bir maskesiz litografi algoritması bu çalışmada gerçekleştirilmiştir. Öne sürülen algoritma dijital holografi ile elde edilen nicel faz görüntülerini kullanarak litografi için kullanılan maskeyi sürekli güncellemektedir. Bu sayede süper çözünürlüklü görüntülemede kullanılan bir spiral faz maskesi üretilip klasik metoda göre daha iyi bir sonuç verdiği gösterilmiştir.

TABLE OF CONTENTS

LIST OF FIGURES

LIST OF TABLES

LIST OF SYMBOLS

c	Speed of light in vacuum
I	Intensity of wave (on image plane)
i	Imaginary number $i = \sqrt{-1}$
k, $\overrightarrow{k}$	Wave vector for light $\lvert k \rvert = \frac{2\pi}{\lambda}$
$\overrightarrow{k}_{rt}$	Wave vector for tilted reference wave
M	Magnification
n	Refractive index for material
o	Complex object wave
r	Complex reference wave
r_p	Fresnel reflection coefficient for p polarization
r_s	Fresnel reflection coefficient for s polarization
r_t	Tilted complex reference wave
t	Time
(x, y)	Spatial coordinates in cartesian coordinate system
Γ	Mutual coherence function
Δx	Pixel size of detector
θ	Off-axis angle or incidence angle for TIR
λ	Wavelength of light
ϕ	Phase angle
Ψ	Complex Field
ω	Spatial frequency
$\mathcal{F}\left\{\star\right\}$	Fourier transform of $\star$
$\mathcal{F}^{-1}\left\{\star\right\}$	Inverse Fourier transform of $\star$
$\lvert\star\rvert$	Magnitude of $\star$
$\widehat{I}$	Fourier transform of the function I
$\circledast$	Convolution operator

a^*	Complex conjugate of a
$\langle\star\rangle$	Averaging function for $\star$

LIST OF ACRONYMS/ABBREVIATIONS

2D	Two Dimensional
3D	Three Dimensional
BFP	Back Focal Plane
CAD	Computer Aided Design
DH	Digital Holography
DHM	Digital Holographic Microscopy
FFT	Fast Fourier Transform
FoV	Field of View
NA	Numerical Aperture
NPL	Numeric Parametric Lens
OPL	Optical Path Length
SLM	Spatial Light Modulator
STED	Stimulated Emission Depletion Microscopy
TIR	Total Internal Reflection
TIRFM	Total Internal Reflection Fluorescence Microscopy
TIRHM	Total Internal Reflection Holographic Microscopy
TIRM	Total Internal Reflection Microscopy
UV	Ultraviolet

1. INTRODUCTION

1.1. Holography

Holography was first developed by D. Gabor in 1948 and brought new possibilities to optics as this method enabled the recovery of the physical wavefront [1–3]. The hologram is created by interference of a reference wave and the diffraction pattern generated by an object. The hologram can later be illuminated by the same reference wave to obtain the image of an object at desired distances. Another recording configuration is proposed by Denisyuk in 1962 [4]. In Denisyuk's configuration, object is placed behind the photosensitive plate at very close distances. The light reflected from object and incoming light creates an interference pattern which creates hologram. However, effective employment of this technique to light waves requires coherent light sources, namely lasers and photo-sensible materials with sufficient dynamic range and resolution. First successful multicolor reflectance holograms are produced by Stroke using Denisyuk configuration in 1966 [5]. Nonlinearity of photoresist, the fixation of diffraction pattern after illumination were still important practical limitations which prevented the wide use of holography. To circumvent these material dependent 'analog' problems, the first concept of digital holography is introduced by Goodman in 1967 [6]. Following the advancement in lasers and digital detectors, digital holography is mainly developed in the 90s [7–12]. The use of digital detectors as recording media removed the requirement for physical recording and enabled recovery of the wavefront in the digital domain by the propagation of fields numerically. The retrieval of complex field, amplitude, and phase became especially useful in imaging biological samples as their amplitude contrast is low because they are mostly transparent, and high-resolution topographic imaging with high z resolution [13–16].

A non-exhaustive list of Nobel prize winners which directly or indirectly contributed to development of digital holography is given in Table 1.1 [17].

1.1.1. Phase Imaging

Digital holography allows recovery of the complex wavefront in terms of amplitude and phase. Unlike other amplitude-based methods, phase recovery opens up new possibilities with mostly transparent materials. This advantage is highly desirable in imaging biological samples as most biological specimens provide weak amplitude contrast. The common imaging devices such as cameras, photodetectors, and the human eye are only sensitive to light intensity, so phase imaging is not a trivial problem. There are other non quantitative methods to measure the phase of the specimen, such as phase-contrast imaging [18, 19], differential interference contrast imaging [20], etc. These methods will be discussed briefly in this section as an introduction to state of the art for phase imaging.

Table 1.1. Nobel prizes in physics which are important for development of digital holography.

Year	**Recipient(s)**	**Awarded for**
1907	Albert Abraham Michelson	Optical precision instruments
1953	Frits Zernike	Invention of the phase contrast microscope
1964	Charles Hard Townes Nicolay Gennadiyevich Aleksandr Mikhailovich Prokhorov	Laser principle
1971	Dennis Gabor	Invention and development of the holographic method
2000	Jack S. Kilby	Invention of the integrated circuit
2009	Willard S. Boyle George E. Smith	Invention of an imaging semi-conductor circuit - CCD sensor

Phase-contrast microscopy was first proposed and developed by F. Zernike in 1934 [21]. This method relies on the interference between non-diffracted wave coming directly from illumination and wave diffracted from the specimen. The phase of specimen is encoded to the intensity contrast which can be recorded by traditional recording devices. The imaging system has a standard illumination with an annular condenser placed at the output. The annular illumination allows the separation of diffracted and non-diffracted beams as shown in Figure 1.1. In this figure the dashed line shows the optical path by diffracted light. To introduce a $\lambda/4$ phase shift in diffracted light to generate interference pattern on imaging plane, a phase plate is placed after the sample on the pupil plane to the non-diffracted wave's optical path. An additional gray filter can be placed on the non-diffracting wave's optical path to match the intensities of waves to utilize the recording device's dynamic range better. The resulting phase contrast image has intensity proportional to the optical path length (OPL) of the specimen.

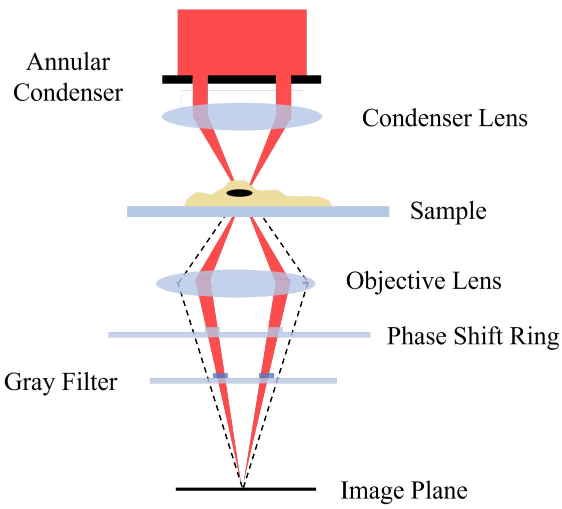

Figure 1.1. Typical phase contrast microscopy setup.

Differential interference contrast microscopy is developed by Nomarski [22, 23]. This method relies on the gradient of phase to create contrast unlike the phase contrast method in which the intensity is proportional to OPL difference across the sample. The illumination light is divided into two orhogonal polarization state by utilizing a Wollaston prism and falls onto sample plane with slight offset in the direction decided by orientation of Wollaston prism. These two rays carry out the phase information of sample at respective points and are recombined before detection to create an interference pattern. The amplitude of interference pattern is proportional to OPL difference between two rays, so effectively creates an image for phase gradient of specimen.

1.1.2. Principles of Holography

Holography was first developed by D. Gabor in 1948 and experimentally demonstrated by electron beams. The motivation behind this work was to image microscopic objects with small wavelength light and reilluminate the recorded hologram with a bigger wavelength to achieve magnification with high resolution. Gabor preferred a holographic approach to achieve this as lenses were not experimentally practical for electron beams. The development of holography improved the spatial resolution for electron beam imaging.

Holography relies on the interference pattern created by two coherent waves. One of the waves comes from the object and carries information of the object and is generally called object wave, whereas the second wave comes from a reference plane and the properties of the reference wave are usually well-known. The interference pattern can be recorded by a photosensitive plate for classical holography or by a digital camera for the case of digital holography. In the classical case, the interference pattern creates a corresponding diffraction pattern on a photosensitive plate, and the object wave can be recovered by illuminating this pattern with the same reference wave. This method enables the recovery of full complex field.

The interference pattern on the sensor can be described as the sum of two perfectly coherent waves with the same polarization. The resulting intensity becomes

$$I(x,y) = |o(x,y) + r(x,y)|^2\,, \tag{1.1}$$

$$= (o+r)\cdot(o+r)^*, \tag{1.2}$$

$$= |o|^2 + |r|^2 + or^* + ro^*. \tag{1.3}$$

Here o corresponds to the complex object wave and r corresponds to the complex reference wave, whereas (x, y) shows the coordinate system on the detector. In Equation

(1.3), the first two terms correspond to the intensity of object and reference beams, respectively, and can be recovered utilizing classical incoherent imaging setups. However last two terms carry out phase information and require a coherent illumination to be recorded.

If two waves are expressed by their amplitude and phase such as $o = |o|\, e^{i\phi_o}$ and $r = |r|\, e^{i\phi_r}$, resulting intensity calculated in Equation (1.1) can be written as

$$I = \left| |o|\, e^{i\phi_o} + |r|\, e^{i\phi_r} \right|^2, \tag{1.4}$$

$$= |o|^2 + |r|^2 + |o|\,|r|\, e^{i(\phi_r - \phi_o)} + |o|\,|r|\, e^{i(\phi_o - \phi_r)}, \tag{1.5}$$

$$= |o|^2 + |r|^2 + 2\,|o|\,|r| \cos(\phi_o - \phi_r), \tag{1.6}$$

$$= I_0 + I_1 \cos(\Delta\phi). \tag{1.7}$$

In Equation (1.7), the $I_0 = |o|^2 + |r|^2$ term corresponds to background intensity whereas $I_1 = 2\,|o|\,|r|$ shows the envelope for phase dependent intensity. According to phase difference, $\Delta\phi$, between the object and the reference wave the total intensity on detector changes. The phase information is encoded in hologram using this property. Although Equation(1.3) looks nice and clean, it is not trivial to recover the initial object field as the last two-term includes one wave and other's complex conjugate multiplied.

For classical holography, the diffraction pattern on the hologram is illuminated by a known illumination for the reconstruction. In the physical model, if we ignore the responsivity of the photorefractive plate, we can see the effect of illumination by multiplication of illuminating complex field, $u(x, y)$, with the recorded intensity I. This process can be expressed mathematically as

$$u \cdot I = u(|o|^2 + |r|^2) + uor^* + uro^*. \tag{1.8}$$

From this equation, it can be seen that the second term is equal to the object wave multiplied with the illumination wave. So recovery of the original field is possible by illuminating the diffraction pattern with a proper and known $u(x, y)$ in theory. However, the last term also carries similar information, complex conjugate of the object wave, which corresponds to a twin image of original object and forms at the opposite side of hologram as depicted in Figure 1.3. If illuminating field is chosen to be same as reference field($u = r$), resulting wavefront will be equal to

$$r \cdot I = r(|o|^2 + |r|^2) + o\,|r|^2 + o^* r^2. \tag{1.9}$$

With this specific choice of u, the third term shows the object multiplied with the amplitude of the reference wave. So theoretically, perfect recovery of original object field is achieved by using a unity magnitude reference wave and a unity magnitude reconstruction beam.

In the next subsection, an experimental implementation of a holography as proposed by Gabor will be explained. The following subsections will focus on twin image problem arises from in-line holography configuration and coherence requirements for holography recording.

1.1.2.1. Lensless Holography. The Equation (1.9) does not assume anything about the optical system and is very general for any kind of holographic recording. The original work of Gabor focuses on lensless imaging, and in this chapter, we will introduce how a lensless holography setup works. In this imaging configuration, a diverging spherical wave illuminates the sample as shown in Figure 1.2. The wave diffracted from the sample, and the non-diffracting wave continues propagating to the recording plane with different radii of curvature, d_o, and d_r respectively, and creates an interference pattern on recording plane under the assumption of weakly scattering object. In this configuration non-diffracted component of the wave acts as a reference beam.

After diffraction patterns form on photosensitive material, the hologram can be illuminated with the same initial illumination to recover the image of original object as expressed in Equation (1.9). This process can be seen in Figure 1.3.

The 2^{nd} term in Equation (1.9) gives the virtual image of object, and 3^{rd} term causes a real image to form in the original position of object. The conjugate image is generally called as the twin image of the image of interest.

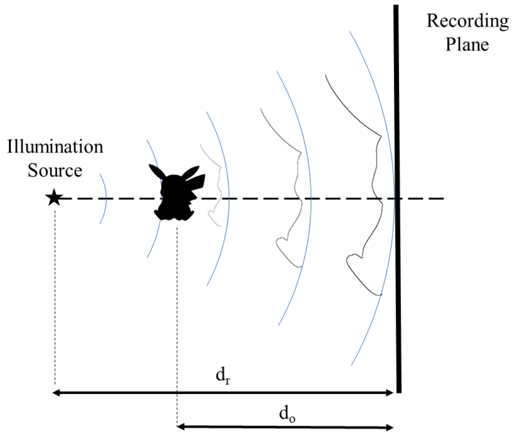

Figure 1.2. Recording configuration for in-line lensless holography.

Although this configuration does not use any lens to recover the original object wave, it is also possible to produce a magnified version of the original object. Magnification can be achieved by using a reference wave with a different radius of curvature between at the steps of recording and reconstruction. This can be implemented by either changing the position of the illumination source or by utilizing a source at a different wavelength. The magnification achieved by these changes can be expressed as [24]

$$M_{lat} = \left| 1 + d_o \left(\frac{\lambda}{\lambda'} \frac{1}{d_r{}'} - \frac{1}{d_r} \right) \right|^{-1}, \tag{1.10}$$

in which d_r and $d_r{}'$ refers to position of illuminations for recording and reconstruction respectively, d_o shows the distance of object to recording plane, and λ ,λ' refers to recording and reconstruction wavelength respectively. For example, if wavelength stays constant through experiments, to magnify an object $d_r{}' > d_r$ should be satisfied.

As one can notice from Figure 1.3, the undesired components from the virtual image and original non diffracted wave continue to propagate with the object wave, which hinders the obtained image quality and resolution for the object. The twin image problem, which arise from this so-called in-line holography configuration can be circumvented by utilizing an off-axis configuration which will be discussed in the following chapters.

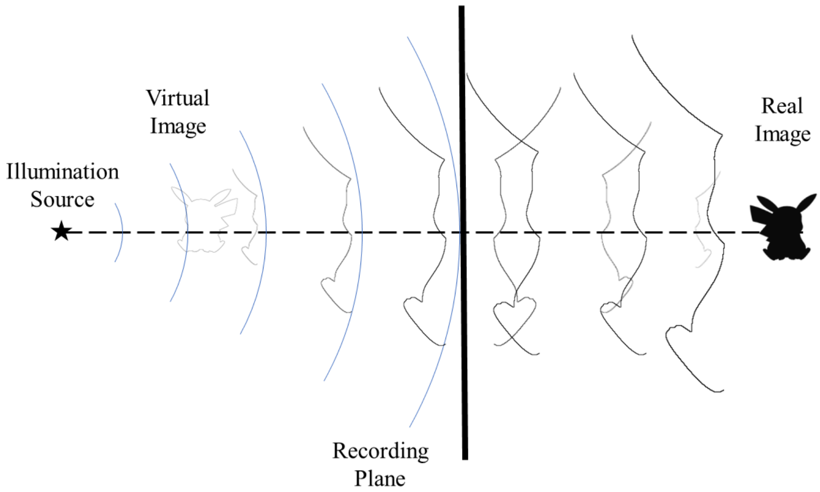

Figure 1.3. Reconstruction configuration for in-line lensless holography.

1.1.2.2. Off-Axis Configuration. The creation of twin image in so-called in-line configuration was the main problem for further development in holography. To decrease the effect of the twin image, using a slightly defocused hologram was proposed by Gabor [2]. However, the main solution to this problem is presented by Upatneiks and Leith, which utilized a reference wave with a slight propagation angle compared to object wave [25]. Since the reference wave is not moving in the system's optical axis (or $\overrightarrow{k}_{ref}$ is not parallel to optical axis) , this configuration is named off-axis geometry. Usage of off-axis beam corresponds to multiplying object wave with a linearly increasing phase function, which shifts the spatial frequency components of the object wave and its conjugate in opposite directions in the Fourier plane. The multiplication with a sine wave to isolate the desired signal was a well-known procedure in signal processing. The off-axis concept was realized again by Leith and Upatneiks [26] in 1964, and first quantitative phase measurement was performed by Carter in 1970 [27].

In Figure 1.4, $\overrightarrow{k_o}$ denotes the wave vector for the object wave, and $\overrightarrow{k_{rt}}$ denotes the wave vector for the reference wave. The angle between the reference and the object wave can be adjusted freely to completely isolate (without aliasing) the cross-correlation terms in Equation (1.9) in Fourier space. The object wave is generally on the optical axis for convenience and corresponds to the ideal recording case.

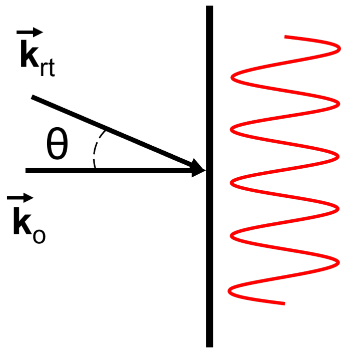

Figure 1.4. Interference pattern formed by off-axis k vectors.

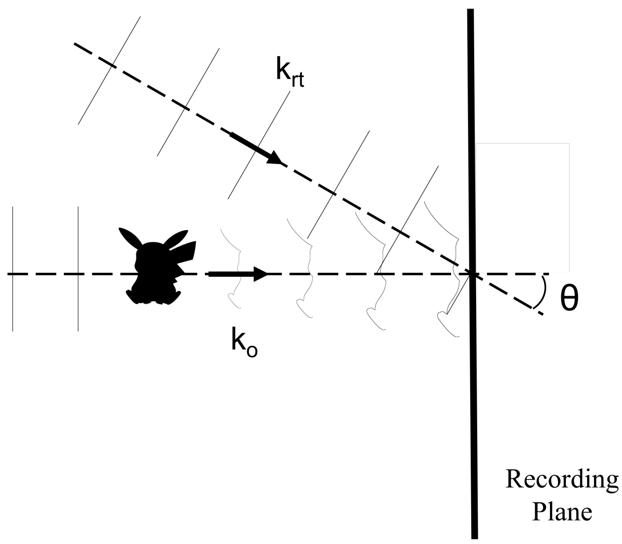

Figure 1.5. Recording configuration for off-axis lensless holography.

Mathematically, tilted reference wave corresponds to the original reference wave multiplied with a linear phase function so that the tilted reference wave can be expressed as $r_t = re^{i\left(\overrightarrow{k_{rt}}\,\overrightarrow{x}\right)}$. Here $\overrightarrow{x} = (x, y)$ shows the position vector in cartesian coordinate system placed on recording plane. If we insert this new r_t value to Equation (1.9) we end up with

$$I = |o|^2 + |r|^2 + o^* r e^{i(\overrightarrow{k_{rt}} \cdot \overrightarrow{x})} + o r^* e^{-i(\overrightarrow{k_{rt}} \cdot \overrightarrow{x})}, \tag{1.11}$$

for intensity on recording plane. The geometry for recording can be seen in Figure 1.5. From the previous equation, we can see that the cross-correlation terms are multiplied with a linear phase which will change their propagation direction hence a chance to negate the effects of the twin image. To reconstruct object wave, the hologram can be illuminated with the conjugate of reference beam, which yields

$$r_t^* I = r_t^* \left(|o|^2 + |r|^2\right) + |r|^2 o^* + o(r^*)^2 e^{-2i(\overrightarrow{k_{rt}} \cdot \overrightarrow{x})}. \tag{1.12}$$

From Equation (1.12), we can see that every term is propagating in a different direction. If the distance between object and recording plane is sufficiently large for a given tilt angle, spatial separation of terms is possible, which removes the effect of twin image and zero-order for reconstructed object wave. The geometry for reconstruction with tilted illumination wave can be seen in Figure 1.6.

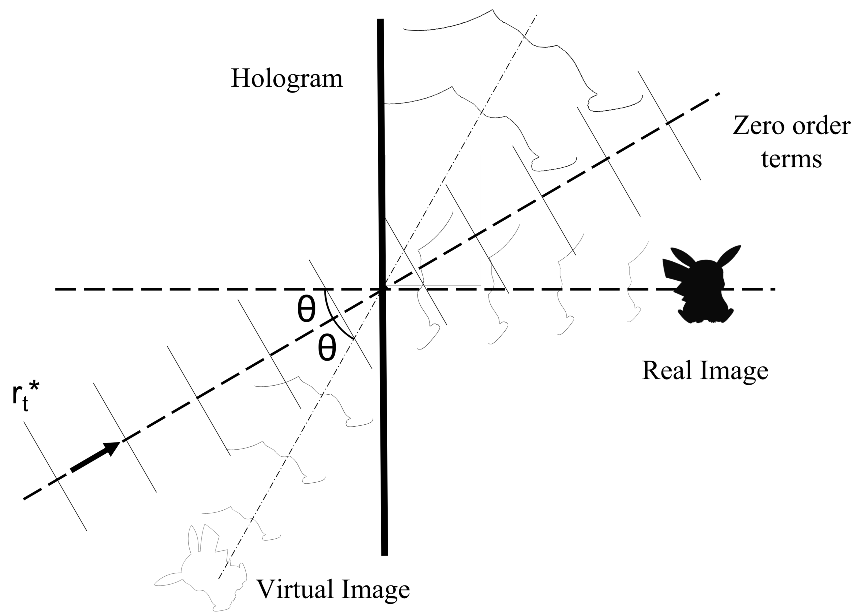

Figure 1.6. Reconstruction configuration for off-axis lenseless holography.

In theory, there is no limitation for tilt angle for the separation of terms. However, experimentally tilt angle is limited by the resolving capability of the medium (grain size, photopolymer definition etc.) and starts becoming a significant limitation, especially for digital holography. The increase in tilt angle creates an interference pattern with a shorter period hence requiring a better resolving capability to be properly sampled on photosensitive film. Holographic films have typical minimum definiton capabilities of thousands of lines per millimeter, allowing tilt angles up to tens of degrees [28].

1.1.2.3. Coherence. For simplicity, up until now, the reference and object wave is considered to be perfectly coherent. Although this assumption can be justified by the development of narrow-band lasers, it is useful to utilize lasers with short coherence length to decrease the effect of parasitic interference coming from reflections in the optical system. The intensity and quality of interference pattern for recording greatly depend on coherence, and coherence can be divided into two parts, spatial coherence, and temporal coherence. This section will cover the mathematical analysis of these two types of coherence. Temporal coherence shows the ability of waves to interfere in the time domain. Experimentally, the difference in propagated optical path length creates a time shift (or temporal shift) in one of the waves. Mathematically temporal coherence can be expressed as

$$\Gamma_{11}(\tau) = \langle u_1^*(t) u_1(t+\tau) \rangle \, . \tag{1.13}$$

For a monochromatic wave, Γ_{11} gets its maximum value. The Γ_{11} tends to be in a gaussian shape and value of it decreases by the increase in bandwidth ($\Delta\lambda$) of light source since temporal behavior of a light source is depends on the Fourier transform of its spectral properties. Thus, a term called coherence time can be defined to show τ_c required to decrease fringe contrast to $1/e$ of its maximal value. From this definition also coherence length can be defined as $L_c = c \cdot \tau_c$. Here c denotes the speed of light in vacuum. So experimentally, it is important to keep optical path length differences to stay below L_c value to get sufficient fringe contrast. This generally brings a requirement to have a delay line to match optical path lengths for object illumination and reference arm.

Spatial coherence, much similar to its temporal counterpart, shows the ability of waves emitted from different points in the same wavefront to interfere. Since they are on the same wavefront, spatial coherence is independent from temporal coherence. Spatial coherence can be expressed as

$$\Gamma_{12}(\mathbf{r}_1 \cdot \mathbf{r}_2) = \langle u^*(\mathbf{r}_1)u(\mathbf{r}_2)\rangle \,. \tag{1.14}$$

Here $\mathbf{r}_1$ and $\mathbf{r}_2$ shows the emission points for waves. Γ_{12} is maximal for a point source and value of Γ_{12} decreases as the size of source increases.

In the early days of the holography, the coherence – temporal and spatial - were the main problem that prevented high-quality holograms as laser technology was not fully matured. This was especially problematic for holography as interference in wide-field is required to generate a hologram and to reconstruct the original field. Experimental effects of coherence can be seen with a slight modification to Equation (1.3),

$$I(x, y) = |o|^2 + |r|^2 + (o^*r + or^*)\, G_{12}(x, y). \tag{1.15}$$

Here $G_{12} \in [0, 1]$ is a weighting term indirectly related to coherence properties of light $\Gamma_{12}(\mathbf{r}_1, \mathbf{r}_2, t)$. For ideal case this weighting term equals to one, and for incoherent illumination it is equal to zero.

The classical common path configuration ensures coherence by utilizing self-diffraction of illumination beam to generate holograms so that optical path difference is close to zero between interfering parts. Also, illumination is done by spatially filtered source which ensures spatial coherence.

1.1.3. Digital Holography

The development of classical holography paved the way for exciting applications such as wavefront recovery and lensless imaging. However, recording a hologram was still troublesome because exposure time had to be carefully adjusted to be in the linear region of photosensitive material. Even then, the nonlinearity of material caused some higher-order diffraction terms to be generated, which eventually increases noise in reconstruction. Also, after illumination, the resulting hologram should be further processed chemically to fixate the diffraction pattern for long-term use and reconstruction, which takes a long time and greatly determines the reconstructed field's quality. The development in electronics opened up the possibility of using digital cameras instead of photosensitive plates for the recording medium. Following the advancements in computation capabilities of computers, digital cameras also allowed reconstruction of wavefront digitally in near real-time. However, sampling capabilities of photosensitive plates are typically ten times higher than current digital cameras, so usage of digital holography has a disadvantage in that regard. But digital holography enables quantitative phase imaging which is not possible in classical holography.

Another possibility opened up with the usage of digital cameras is the employment of phase-shifting techniques for the recovery of the wavefront. This technique utilizes the quick acquisition times of digital cameras to temporally encode phase information on hologram instead of spatial encoding like in an off-axis configuration. This requires multiple frames to process with known phase shifts but is able to use the whole frequency range camera can offer or, for a similar resolution, have larger FoV compared to single-shot methods. The requirement for multiple frame decreases the temporal resolution or rate of the phase images captured by the system. Also temporal variations in specimen with phase shifted images causes imperfections.

The main goal of classical holography was to image an object without a lens or construct the original wavefront. Development of digital methods enabled the recovery of phase of specimen in addition to amplitude and turned digital holography into one of the first quantitative phase imaging methods [14]. Phase imaging has found its applications, in characterization of optics and microsystems, and biological sciences, with its observation capabilities and widefield topographic measurements with high resolution.

The general experimental setups for digital holography can be divided in to two groups, reflection and transmission configuration. Although the acquisition and reconstruction steps are similar for both groups, the interpretation of the phase acquired depends on which geometry is used. For transmission geometry (Figure 1.7, 1.9), the amplitude of the recovered wave gives the transmission map of investigated object, and the phase of the recovered wave gives the integrated optical path length along the illumination direction (Equation (1.16)). For reflection geometry (Figure 1.8, 1.10), the amplitude of the recovered wave gives the reflection coefficient of the reflective surface, whereas the phase is proportional to the height distribution (or topography) of the sample (Equation (1.17)),

$$\phi_{trans} = \int_0^{h(x,y)} \frac{2\pi}{\lambda} n_m(x, y, x) dz, \tag{1.16}$$

$$\phi_{refl} = \frac{2\pi}{\lambda} n_i \cdot 2 \cdot h\left(x, y\right). \tag{1.17}$$

Here n_i is the refractive index of environment, $n_m(x, y, z)$ is the refractive index distribution of sample, $h(x, y)$ is the height distribution of sample, and λ is the wavelength of light used for detection. For biological applications, since most of the samples are highly transparent, generally a transmission configuration is used. The thickness of cells can be estimated assuming a constant refractive index through cell [29] or total phase (ϕ_{trans}) can be used to calculate dry mass of cell to measure for example growth rate of a cell colony [30, 31].

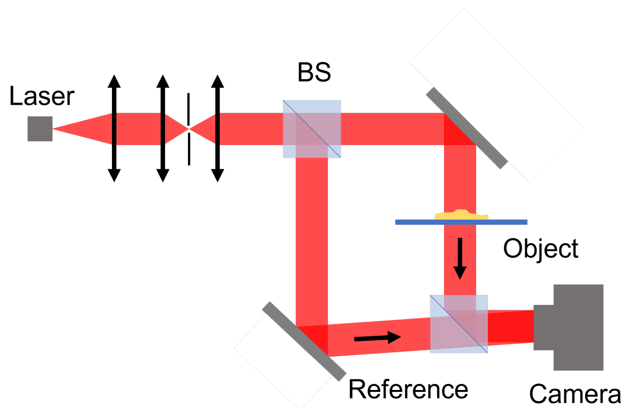

Figure 1.7. A typical lensless off-axis holography setup for transmission recording.

Depending on desired magnification and resolution, the system can directly image the sample without an additional lens with unity magnification or by magnifying the sample by combining the microscope objective and tube lens, which can be seen in Figure 1.9, 1.10.

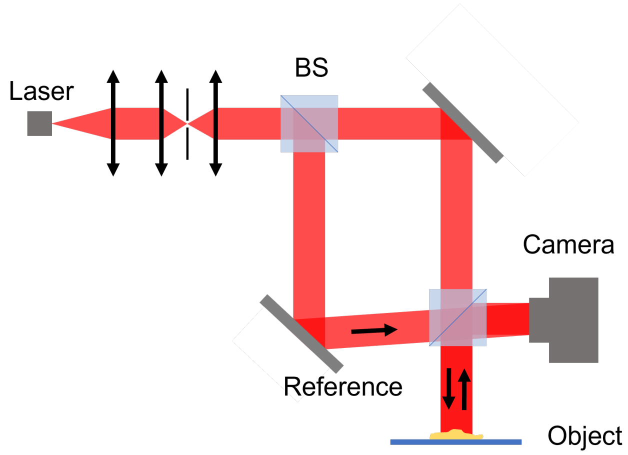

Figure 1.8. A typical lensless off-axis holography setup for reflecting samples.

For all combinations, to ensure a homogeneous illumination on sample, spatial filtering can be applied to the light source, increasing the spatial coherence. Then collimated beam can be divided into two by a beam splitter to be used in the object and the reference arms. After the object beam passes through the sample or reflects from the sample, it falls on to the detector. For off-axis configuration, the incidence angle for the reference beam can either be adjusted by a mirror or by placing a second beam splitter with an offset angle. A condenser lens (C) is placed in the object arm to focus light to the back focal plane of the microscope objective (MO) to create brightfield illumination for microscopic reflection setups but is optional for transmission setups. The scattered light again is collected by the same MO and imaged on camera with a tube lens. To match the curvature of the object and reference beam, a curvature lens can be placed in the reference arm. The camera can be directly placed in the image plane or placed with a slight offset from the image plane. For microscopic transmission setups, a condenser can be placed before the sample to reduce unwanted diffraction effects if beam sizes are not optimal. Then the sample is imaged onto the image plane with the help of a microscope objective and a tube lens similar to the reflection case. For Figure 1.9 and 1.10, the dashed lines show the path for the diffracted beam.

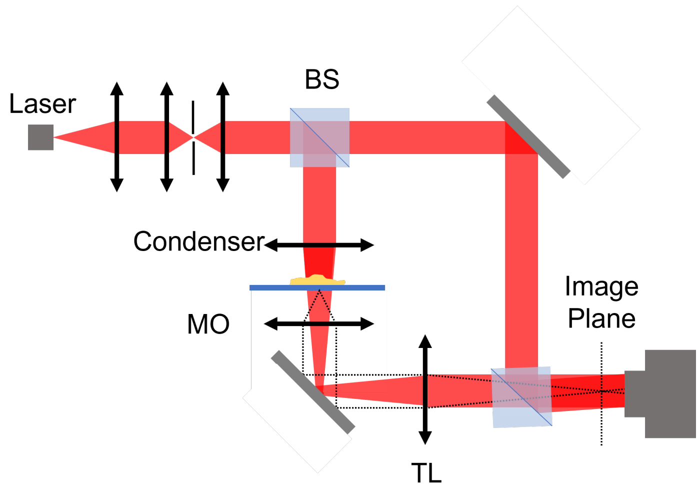

Figure 1.9. A typical off-axis holography setup for transmission recording with magnification.

<u>1.1.3.1. Light Sources.</u> When the holography was first developed in the 40s, finding adequate light sources which satisfy coherence length conditions was a big problem. At first, filtered mercury lamps were used as illumination sources [2, 26]. Following the advancement of lasers, the use of lasers became the standard in the field with their easy accessibility and long coherence lengths. Light-emitting diodes are also used in literature to take advantage of their low coherence length to reduce coherence noise. One can use widely available spatial filters with desired pinhole diameter to ensure spatial coherence at the expense of intensity loss. Utilizing fibers to create the object and reference beams is also a possibility that intrinsically incorporates spatial filtering. Fiber usage allows one to change illumination sources quickly to find the best laser with spectral bandwidth to use in holography. To sum up, if there is enough intensity for the camera to detect after beam processing, and the light source satisfies spatial and temporal coherence requirements with a defined polarization state, any light source can be used as illuminator for hologram recording.

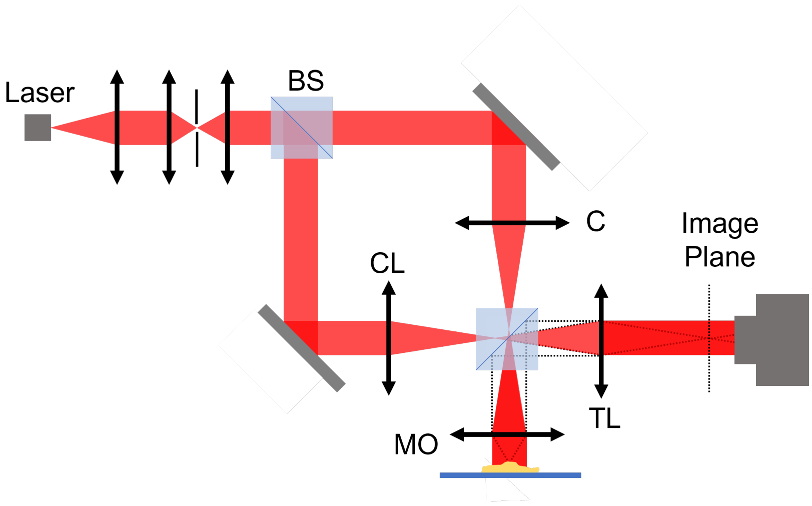

Figure 1.10. A typical off-axis holography setup for reflecting samples with magnification.

1.1.3.2. Off-Axis Angle. There are two main configurations that allow one to recover the full wavefront without a twin image. The first one of these methods utilizes an in-line configuration in which the object and reference beam is propagating on the same optical axis. The phase of the reference wave is shifted by a known amount to obtain multiple interference pattern on the camera. These images can then be combined in a specific fashion described by Zhang [32] to recover the object wave, which requires multiple frames but can potentially benefit from the full space bandwidth product that the camera can offer. The second method uses an off-axis configuration in which, generally, the object wave propagates along the optical axis of the system, and the reference beam propagates in an axis with a tilt angle with respect to the object wave (or off-axis). To fully replicate the object wave, one must be careful about eliminating aliasing effects to isolate the object wave in Fourier space properly. This requirement sets a limit to minimum tilt angle, whereas the camera's pixel size limits the maximum tilt angle. We can assume that the reference beam is a plane wave for the ideal case. Under this assumption, if we take use properties of Fourier transform to take Fourier transform of Equation 1.11, Fourier transform of first term equals to

$$\mathcal{F}\left\{|o|^2\right\} = \mathcal{F}\left\{o \cdot o^*\right\} = \widehat{o} \circledast \widehat{o}^*. \tag{1.18}$$

Here we utilized the multiplication property of Fourier transform. The Fourier transform of second term in Equation 1.11 gives

$$\mathcal{F}\left\{r\right\} = R \cdot \delta\left(\omega\right), \tag{1.19}$$

as the reference wave is assumed to be plane wave. The Fourier transform of third term corresponds to a shift in Fourier domain,

$$\mathcal{F}\left\{o \cdot e^{-i(\omega_0 r)}\right\} = \widehat{o}\left(\omega + \omega_0\right). \tag{1.20}$$

Finally if we combine all the terms we end up with

$$\widehat{I}(\omega_x, \omega_y) = \widehat{o} \circledast \widehat{o}^*(\omega) + R^2\delta(\omega) + R\widehat{o}(\omega + \omega_0) + R\widehat{o}^*(\omega - \omega_0), \tag{1.21}$$

where ω denotes the angular frequency and has dimension of m^{-1}. In Equation (1.21), $\omega_0 = (\omega_{0x}, \omega_{0y})$ is the frequency modulation created by the interference pattern caused by the off-axis illumination.

For an optically limited system, if the spectral limit of the system is imposed by a circular aperture(for example, NA of microscope objective), typically, one can see Figure 1.11 for the Fourier transformed version of the hologram.

In this figure ω_b shows the radius for spectral bandwidth of the system and for unity magnification system can be written as

$$\omega_b = 2\pi\frac{NA}{\lambda}. \tag{1.22}$$

NA shows the numerical aperture for limiting structure in the optical setup. The 0-order term has a radius of $\omega_a = 2 \cdot \omega_b$ because 0-order term is just the multiplication of object beam with itself. Multiplication in the spatial domain equals convolution in the Fourier domain. So spectral bandwidth of the 0-order wave is twice of the original object wave. Distance between center of +1 order and 0-order in Fourier space is denoted by ω_0 and is related to tilt angle by the relation

$$|\omega_0| = 2\pi\frac{\sin\theta}{\lambda}. \tag{1.23}$$

Size of the Fourier domain is limited by the pixel size of camera. For a pixel size of Δx, the maximum frequency which can be distinguished by the camera equals to $\omega_{x,max} = 2\pi\frac{1}{2\Delta x}$ by the Nyquist theorem. The zero aliasing requires no overlap between +1 (or -1)order term with 0-order term in frequency domain which enforces a lower bound for the value of $|\omega_0|$

$$|\omega_0| = 2\pi\frac{\sin\theta}{\lambda} > 3\omega_b. \tag{1.24}$$

The upper limit for ω_0 in a diagonal direction can be found by considering +1 order term placed with its borders touching to the limits of Fourier space. To be able to cover all frequency components of +1 order, the center of this term should be at least $\omega_b\sqrt{2}$ away from the corner which puts an upper limit to ω_0 as

$$\omega_0 < \omega_{x,max}\sqrt{2} - \omega_b\sqrt{2}. \tag{1.25}$$

As long as these two conditions are satisfied one can fully reconstruct the object wave. Another constraint for tilt angle comes from the coherence requirement for an interference pattern to form. Because propagation directions are different for the reference and the object beams, it is impossible to fully intersect two coherence volumes exactly, as can be seen in Figure 1.12.

For a good quality hologram and consequently low noise phase image, we want to be able to distinguish fringes in the FoV with high contrast. Since the length of detection area in one direction is equal to $N\Delta x$, this brings us another condition for θ

$$\tan\theta \leq \frac{L_c}{N\Delta x\sqrt{2}}. \tag{1.26}$$

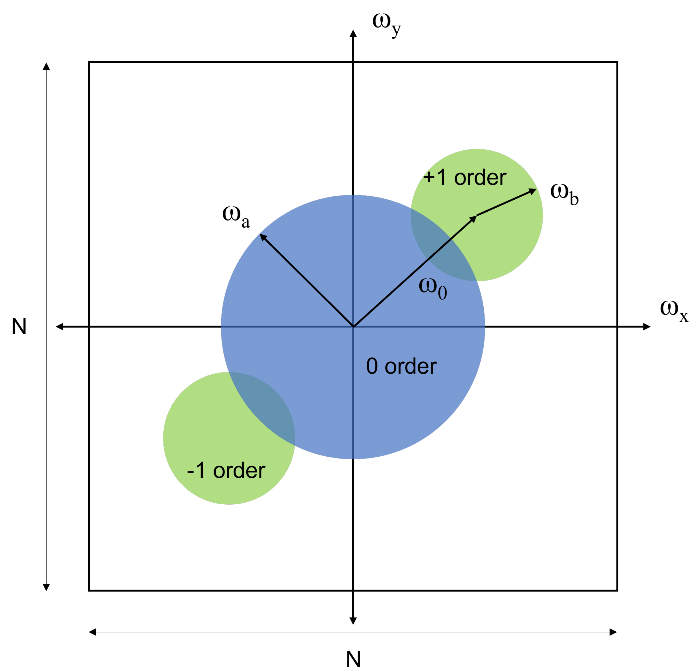

Figure 1.11. Typical organization of interference terms in Fourier space for an optically limited recording configuration.

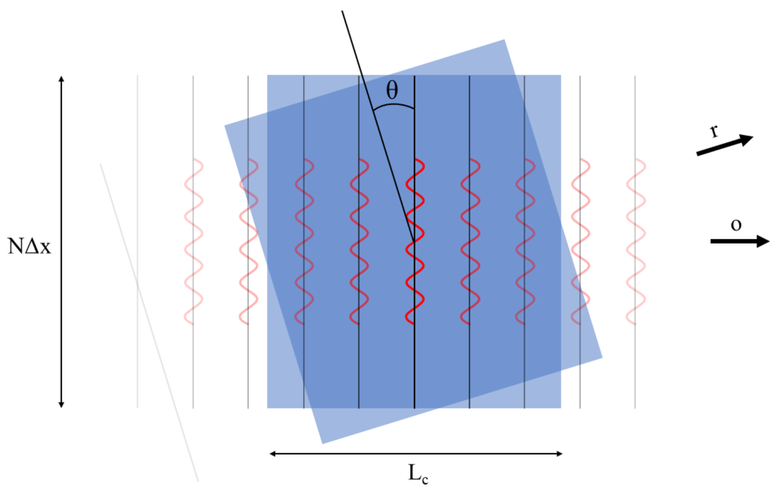

Figure 1.12. Overlap of coherence zones in off-axis configuration.

1.1.4. Reconstruction

We have seen from the previous sections that the off-axis configuration allows object wave to be reconstructed without the effects of zero-order terms or twin image. Classically separation of images is done by propagating hologram with some amount such that twin image and zero order terms do not overlap with the image of interest in the spatial domain. However, beam propagation is not desired from a computational perspective because of edge effects. The finite size of the initial matrix causes ripples in directions perpendicular to image edges which disrupt the quality of obtained phase image. To decrease edge effects, one can use a bigger initial matrix to see effects at larger propagation distances. This is not desired as most reconstruction (or propagation) algorithms utilize 2D Fourier transform and computational cost of 2D Fourier transform scales with $n^2 \log(n)$. Here n shows the element number in one row of a square matrix.

From Figure 1.11, we know that the object wave is also isolated in the Fourier domain; given that the tilt angle is chosen to prevent aliasing, we can retrieve the object wave with no propagation if the camera sensor is placed on the image plane. The concept of utilizing Fourier filtering after modulation is applied to a signal was first developed by Takeda et al. [33] for interferometric topography. This method was later generalized and applied in digital holography by Cuche et al. [14] for recovery of phase and amplitude.

The main advantage of Fourier filtering comes from the fact that it can reconstruct wavefront with a single hologram acquisition. It is robust against vibrations in the optical setup. However, since we are using only a small part of the spectral bandwidth of the camera, we are losing either resolution or field of view compared to multi-shot methods. After filtering, the recovered object wave can be expressed as

$$\Psi(x,y) = or^* = \mathcal{F}^{-1}\left\{\mathcal{F}\left\{I(x,y)\right\} \cdot \widehat{W}(x,y)\right\}, \tag{1.27}$$

$$\widehat{W}(\omega_x, \omega_y) = \begin{cases} 1, (\omega_x - \omega_{0,x})^2 + (\omega_y - \omega_{0,y})^2 \leq \frac{\Delta\omega_0^2}{4} \\ 0, (\omega_x - \omega_{0,x})^2 + (\omega_y - \omega_{0,y})^2 > \frac{\Delta\omega_0^2}{4} \end{cases}. \tag{1.28}$$

Here $\widehat{W}$, shows the spectral filter applied in Fourier domain and Δw_0 denotes the diameter of filter. The case expressed in Equation (1.27) and Equation (1.28) is for an optically limited system with equal pixel size and pixel number in both directions as the filter is circular. Although Fourier filtering enables easy recovery of the object field, the finite size of the Fourier domain introduces a rippling effect especially prominent towards the edge of image. So for the recovery, windowing functions can be used to smooth out the edge effects [34, 35].

From Equation (1.28) one can notice that the filtering function $\widehat{W}$ is not centered in Fourier domain. So if the object wave is reconstructed directly after $\widehat{W}$ is applied, a linear phase modulation coming from the carrier frequency will be present in the recovered field. An additional multiplication is required to demodulate the effect of carrier frequency from object wave, which mathematically equals multiplying phase image with a linear phase such that

$$\Psi_H(x, y) = \Psi(x, y) \cdot e^{i(k_x x + k_y y)}, \tag{1.29}$$

$$k_x = \frac{2\pi}{\lambda} \sin\theta \cos\phi, \tag{1.30}$$

$$k_y = \frac{2\pi}{\lambda} \sin\theta \sin\phi. \tag{1.31}$$

Here θ is the off-axis angle between object and reference beam, and ϕ is the azimuthal angle such that $\phi = \arctan\left(\frac{\omega_{0,y}}{\omega_{0,x}}\right)$. From a computational perspective, multiplication with a linear phase is equal to shifting in the Fourier domain. However, it has been shown that finding the linear phase using fitting methods and multiplying the recovered wavefront by the appropriate linear phase is generally more accurate as fitting enables subpixel shifting effectively in the Fourier domain [36].

1.1.4.1. Numeric Parametric Lens (NPL). Multiplication with a linear phase as described in Equation (1.29) can be generalized to compensate for all kinds of aberrations present in the system [36]. This is critical for the performance of quantitative phase imaging as phase is classically more sensitive to aberrations than intensity. In addition to classical aberration sources for imaging setups, curvature mismatch between reference and object wave can manifest itself as a phase curvature in the obtained phase image. However, different types of aberrations can be compensated if we combine phase curvature correction with numerical propagation to reach to the input plane. Mathematically, one can generalize Equation (1.29)

$$\Psi_H(x,y) = \Psi(x,y) \cdot \exp\left(ik \sum_{m=0}^{M} \sum_{n=0}^{N} C_{mn} x^m y^n \right). \tag{1.32}$$

Here C_{mn} represent aberration coefficients in the cartesian coordinates system, but any other orthogonal basis can be used for aberration correction. C_{10} and C_{01} corresponds to linear phase corrections as described in Equation (1.29), whereas C_{20} and C_{02} corresponds to spherical aberration coming from curvature mismatch. Although this method is very powerful, it requires a known flat surface on the specimen for phase curvature characterization.

1.1.4.2. Reference Hologram Method. Another method for phase curvature correction is using a reference hologram for phase correction, which requires a hologram obtained from an empty (or flat) field of view. After Fourier filtering, recovered field contains wavefront deformation coming from the optical system. Deformation compensated object wave can be recovered by simply doing a complex division with a reference hologram

$$\Psi_H(x,y) = \frac{\Psi(x,y)}{\Psi_{ref}(x,y)} = \left| \frac{\Psi(x,y)}{\Psi_{ref}(x,y)} \right| \exp\left(i\left[\phi(x,y) - \phi_{ref}(x,y)\right]\right). \tag{1.33}$$

The subtraction term in exponential corresponds to deformation compensation in phase, and the amplitude division corresponds to the amplitude normalization for obtained hologram. The amplitude normalization can also be employed by just taking the intensity image of the object by blocking the reference beam. However, amplitude normalization is not necessary when only phase correction is desired. Since imperfections in optical setup are reproducible, phase aberrations obtained from the different empty fields of views can be averaged for phase compensation [37, 38].

1.1.4.3. Numerical Propagation. If the detector is not placed directly on the image plane of the optical system, as in the case of lensless holography, it is necessary to propagate obtained field to recover the object wave at focus. Although classically, this propagation was done through physical media such as illuminating the diffraction pattern, development in digital holography and computation power of computers enabled propagation calculations to be done digitally.

There are different methods for wave propagation, such as angular spectrum method, Fraunhofer approximation, Fresnel approximation, etc. The most commonly used method is Fresnel approximation derived from Fresnel-Kirchoff diffraction integral as described by Goodman [24]. Fresnel approximation relies on propagation distance being much bigger than the wavelength ($d \gg \lambda$), which is generally the case for optical systems. According to this approximation, the phase of the wave in the image plane can be written as [39]

$$\Psi_I(x, y, d) = \frac{e^{ikd}}{\lambda d} \iint \Psi_H(\xi, \eta) \exp\left(i\frac{\pi}{\lambda d}\left[(x-\xi)^2 + (y-\eta)^2\right]\right) \cdot d\xi \cdot d\eta. \tag{1.34}$$

Here $\Psi_H(\xi, \eta)$ is the recovered field in the recording plane, d is the propagation distance, and (x, y) is the cartesian coordinates on the image propagated plane. The terms of Equation (1.34) can be arranged to allow Fourier transform to be used for the calculation of integral

$$\begin{aligned}\Psi_I(x, y, d) = \frac{e^{ikd}}{\lambda d} e^{i\frac{\pi}{\lambda d}\left(x^2+y^2\right)} \iint \Psi_H(\xi, \eta) \exp\left(i\frac{\pi}{\lambda d}\left[\xi^2 + \eta^2\right]\right) \\ \exp\left(i\frac{2\pi}{\lambda d}\left[x\xi + y\eta\right]\right) \cdot d\xi \cdot d\eta,\end{aligned} \tag{1.35}$$

$$\Psi_I(x, y, d) = \frac{e^{ikd}}{\lambda d} e^{i\frac{\pi}{\lambda d}\left(x^2+y^2\right)} \mathcal{F}\left\{\Psi_H(\xi, \eta) \exp\left(i\frac{\pi}{\lambda d}\left[\xi^2 + \eta^2\right]\right)\right\}. \tag{1.36}$$

This expression of Fresnel approximation allows Fast Fourier Transform (FFT) algorithms to speed up the calculations from a computational perspective for discreet space. Although propagated field can be calculated using Fresnel approximation in this form, one can see that the spatial frequencies used to take Fourier transform $\left(\omega_x = \frac{\xi}{\lambda d}\right)$ change with propagation distance. This changes the so-called pixel size of the propagated field $\left(\Delta x = \frac{\lambda d}{\Delta \xi}\right)$ since is constant and equal to the pixel size of digital camera. However, one can use convolution formalism to express Equation (1.34) as [40]

$$\Psi_I(x, y, d) = \frac{e^{ikd}}{\lambda d} \left[\Psi_H(\xi, \eta)\right] \circledast \left[\exp\left(i\frac{\pi}{\lambda d}\left[\xi^2 + \eta^2\right]\right)\right], \tag{1.37}$$

$$\Psi_I(x, y, d) = \frac{e^{ikd}}{\lambda d} \mathcal{F}^{-1}\left\{\mathcal{F}\left\{\Psi_H(\xi, \eta)\right\} \cdot \mathcal{F}\left\{\exp\left(i\frac{\pi}{\lambda d}\left[\xi^2 + \eta^2\right]\right)\right\}\right\}. \tag{1.38}$$

To be more computationally effective Equation (1.37) can be written as Equation (1.38) which utilizes well optimised FFT algorithms and takes advantage of convolution theorem in Fourier transform. This method keeps pixel size constant through all propagation distances, however is more computationally costly as it generally requires two FFT calculations.

1.2. Total Internal Reflection

Total internal reflection (TIR) is the optical phenomenon that occurs when light coming from a medium with a high refractive index to a medium with a low refractive index totally reflects if the incidence angle is bigger than a critical value. Although Kepler first described this phenomenon in 1611, the theory was completed by Fresnel in 1821, including phase shift obtained from reflections. The critical angle can be found from Snell's Law and equals to $\theta_c = \arcsin\left(n_2/n_1\right)$. Here n_1 and n_2 shows the refractive index for the first and second medium, respectively. According to Snell's Law, the behavior of light can be seen in Figure 1.13. Although the light is totally reflected from the surface separating the two mediums, a non-propagating and non-energy carrying evanescent wave that decays very fast emerges in the second medium, typically in $1/3\lambda$.

Although there is no propagating wave in the second media, the evanescent wave can still be absorbed by dye molecules and cause fluorescence. Also, the phase and amplitude of the reflected wave can still be affected from refractive index inhomogeneities found in second media as expressed by Fresnel equations which will be discussed in Section 1.2.3. The shallow penetration depth makes TIR a suitable candidate for the study of interface structures.

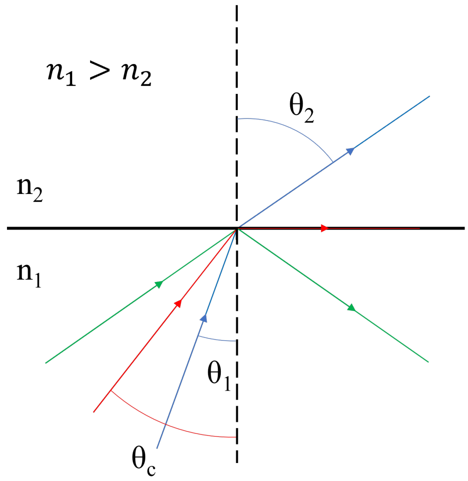

Figure 1.13. Refraction and reflection of light for different incidence angles according to Snell's Law.

1.2.1. Total Internal Reflection Fluorescence Microscopy (TIRFM)

Total internal reflection fluorescence microscopy(TIRFM) was first developed by Axelrod in 1981 [41] to study cell-substrate contact more closely. The excitation laser has an incidence angle larger than the critical angle for the glass-cell medium interface, so it is totally reflected. However, an evanescent wave, which decays exponentially with distance to the interface, can still excite fluorophore molecules inside/on the cell membrane. The fluorescence signal can then be collected by a microscope objective for imaging purposes, as depicted in Figure 1.14. Typical penetration depth for the evanescent wave is in the order of few hundred nanometers. The main advantage of TIRFM is that since mainly fluorescence dyes close to the cell glass border are excited, the background signal coming from other fluorescence molecules spread in the cell is lower than classical epi-illumination [42, 43]. Since a lower number of molecules are being excited by laser, the effect of photobleaching also decreases, enabling extended imaging times for biological samples. Although TIRFM has excellent selectivity, it has some shortcomings in giving a general topography of cell membrane.

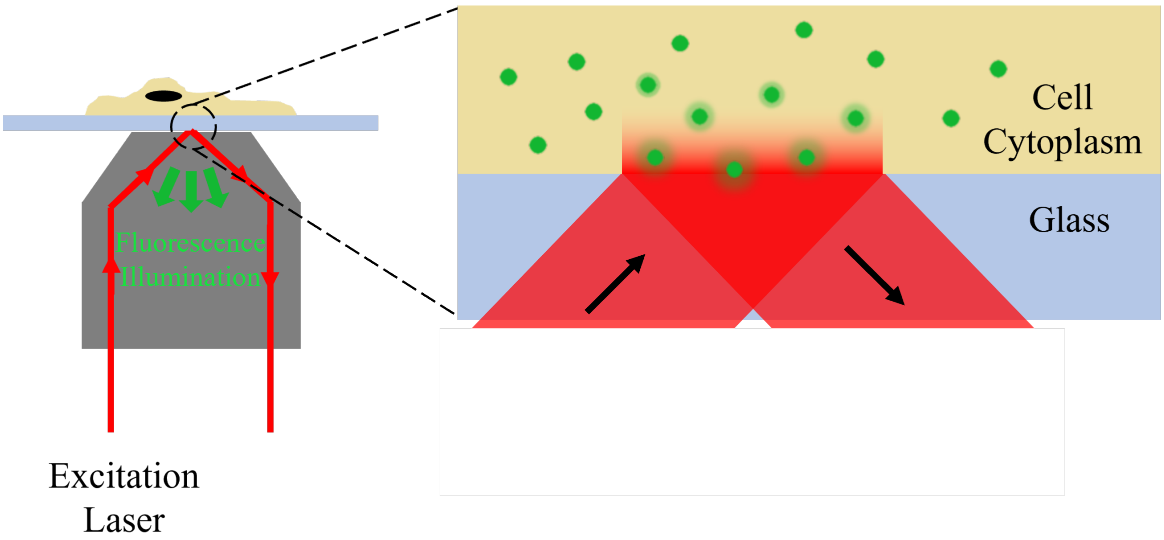

Figure 1.14. Objective based TIRFM illumination and detection.

The first system developed by Axelrod is designed as an addition to an already present imaging system. To create TIR illumination, a prism that is in contact with the specimen is placed under the sample. Evanescent wave excites fluorophores embedded in cells to produce a signal similar to dark field microscopy.

1.2.2. TIR Microscopy

Total internal reflection microscopy(TIRM) was first realized by Ambrose in 1956 to study the surface contact formation of moving cells [44]. In his work, a light with an incidence angle greater than the critical angle for glass-water interface illuminates the sample which is totally reflected from interface. Suppose an object with a refractive index slighty larger than water is in close proximity to the interface. In that case, the total internal reflection becomes 'frustrated', and the amplitude of reflected light decreases at the point of contact. Utilizing this property, Ambrose proposed two main configurations for total internal reflection microscopy: dark-field and bright-field.

An experimental setup for dark field configuration can be seen in Figure 1.15. For this configuration, the sample is illuminated by light that experiences TIR from the glass-water interface. The evanescent wave produced by TIR couples out in the presence of cell contact in an illuminated area. The scattered light then can be collected by a microscope objective to create a TIRM image of the specimen. The bright spots in the image show the points of contact for cells.

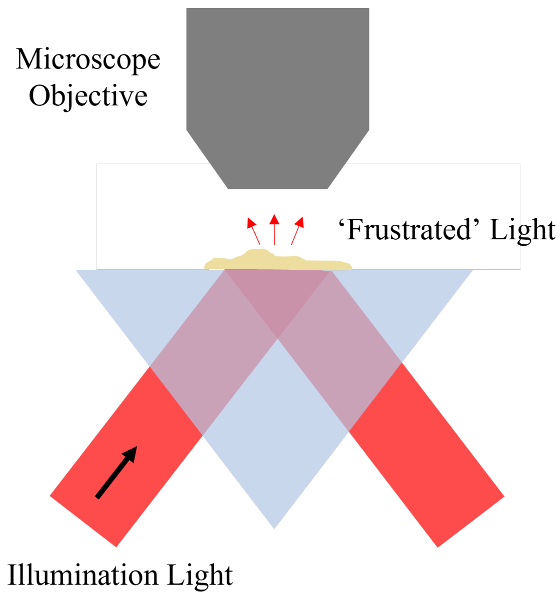

Figure 1.15. Dark-field configuration for TIRM.

Microscope objective is placed in the reflection path for illumination light for bright field configuration as shown in Figure 1.16. The TIR gets frustrated in the areas where the cell is in close contact with glass, so these spots show as dark areas when imaged by the objective. Although this early example utilizes the 'binary' signal to detect contact areas, one can assess the distance between glass-water interface and cell membrane by looking at the amplitude of reflected light with the assumption of a known refractive index. The intensity of an infinitely wide evanescent wave can be expressed mathematically as

$$I(z) = I_0 e^{-\frac{z}{d}}. \tag{1.39}$$

Here z represents the distance between object and interface, and d,

$$d = \frac{\lambda_0}{4\pi} \frac{1}{\sqrt{n_1^2 \sin^2 \theta - n_2^2}}, \tag{1.40}$$

for the TIR case. Using this reflected light intensity dependence on distance, Prieve measured the distance between colloidal particles with a axial resolution of one nm [45].

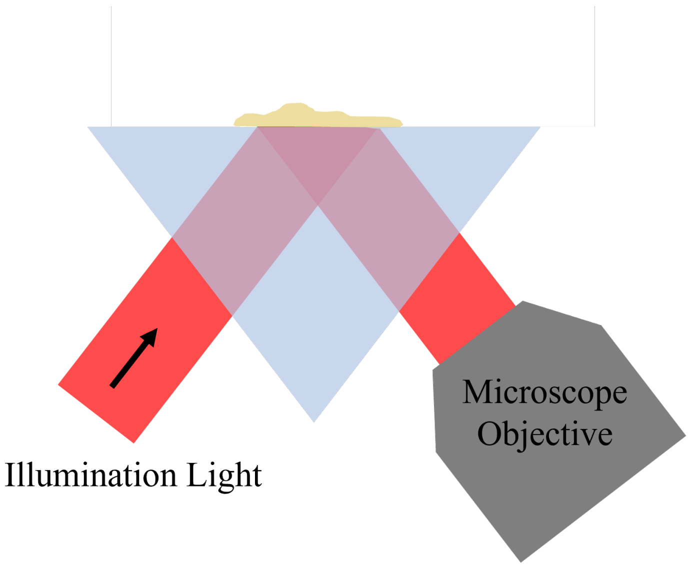

Figure 1.16. Bright-field configuration for TIRM.

1.2.3. Fresnel Coefficients

Although the TIR can be seen from Snell's Law, a complete explanation of phenomenon can be understood using Fresnel's reflection coefficients, including phase shifts. For s-polarization (r_s) (TE mode) and p-polarization (r_p) (TM mode) reflection coefficients are [46]

$$r_s = \frac{n_1 \cos\theta_i - n_2 \sqrt{1 - \left(\frac{n_1}{n_2}\sin\theta_i\right)^2}}{n_1 \cos\theta_i + n_2 \sqrt{1 - \left(\frac{n_1}{n_2}\sin\theta_i\right)^2}}, \tag{1.41}$$

$$r_p = \frac{n_1\sqrt{1-\left(\frac{n_1}{n_2}\sin\theta_i\right)^2} - n_2\cos\theta_i}{n_1\sqrt{1-\left(\frac{n_1}{n_2}\sin\theta_i\right)^2} + n_2\cos\theta_i}. \tag{1.42}$$

Here n_1 is the index of refraction for first medium, n_2 is the index of refraction for second medium, and θ_i is the incidence angle for the incoming wave. The amplitude of reflected wave can be found by squaring the reflection coefficients

$$R_s = |r_s|^2\,, \tag{1.43}$$

$$R_p = |r_p|^2\,. \tag{1.44}$$

For the TIR case ($n_2 > n_1 \sin\theta_i$), the reflection coefficients turn into complex values. These complex reflection coefficients can be written as

$$r_s = \frac{n_1\cos\theta_i - in_2\sqrt{\left(\frac{n_1}{n_2}\sin\theta_i\right)^2 - 1}}{n_1\cos\theta_i + in_2\sqrt{\left(\frac{n_1}{n_2}\sin\theta_i\right)^2 - 1}} = \exp\left(-i2\phi_s\right), \tag{1.45}$$

$$r_p = \frac{in_1\sqrt{\left(\frac{n_1}{n_2}\sin\theta_i\right)^2 - 1} - n_2\cos\theta_i}{in_1\sqrt{\left(\frac{n_1}{n_2}\sin\theta_i\right)^2 - 1} + n_2\cos\theta_i} = -\exp\left(-i2\phi_p\right). \tag{1.46}$$

Here ϕ_s and ϕ_p denotes the phase obtained by reflected wave and equals to

$$\phi_s = \arctan\left(\frac{\sqrt{(n_1\sin\theta_i)^2 - n_2^2}}{n_1\cos\theta_i}\right), \tag{1.47}$$

$$\phi_p = \arctan\left(\frac{n_1\sqrt{(n_1\sin\theta_i)^2 - n_2^2}}{n_2^2\cos\theta_i}\right). \tag{1.48}$$

The plotted graph for reflectance (R) and phase for glass-water and glass-air interface can be seen in Figure 1.17 and Figure 1.18. The TIR starts when the amplitude of reflected wave is equal to 1. This requirement corresponds to an incidence angle of 41.21° for glass-water interface, and 61.18° for glass-water interface. From reflectance graphic we can also see the brewster angle,in which the reflectance for p polarization completely vanishes. The phase shift of reflected wave depends on refractive index ratio of two media and polarization for incoming wave. For these figures, the refractive index for glass, water, and air is assumed to be 1.518,1.33 and 1, respectively.

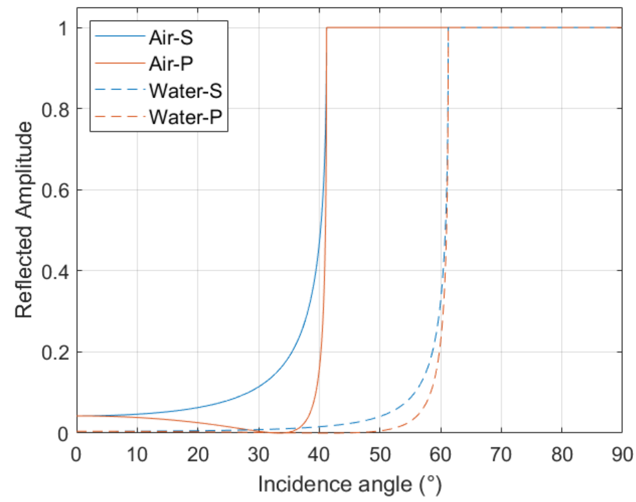

Figure 1.17. Reflectance coefficients for glass-air and glass-water interface for s and p polarizations.

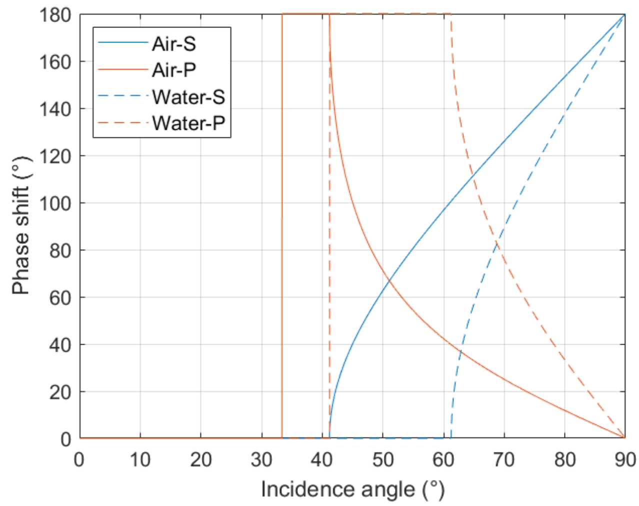

Figure 1.18. Phase shift obtained from TIR for glass-air and glass-water interface for s and p polarizations.

In theory, it is possible to design a system, which measures the phase change of reflected light to measure the refractive index of an object immersed in a medium with known refractive index. The precise position of the object is also can be found from the amplitude of reflected as in TIRM. The additional phase information of phase, helps to characterize the object embedded in the medium.

The digital holography (DH) allows us to measure phase of wavefront quantitatively. So one can combine DH with TIRM for refractive index measurements, or to obtain topography of immersed object. Combining TIR with DH was first done by Ash et al. in 2008, and this new imaging modality is called total internal reflection holographic microscopy (TIRHM). A more in depth examination for TIRHM is given in Section 2.

2. Total Internal Reflection Holographic Microscopy (TIRHM)

2.1. State of the art TIRHM

The first TIR Holographic Microscope (TIRHM) was developed by Ash et al. in 2008 [47]. This early example utilizes a prism to achieve TIR on sample, limiting the working distance of objective to be large and resulting in poor spatial resolution compared to conventional imaging systems. However, this work showed that TIRHM could be used as a complementary tool for widely used TIRF as it has the potential to recover the surface topology of specimen.

The availability of high NA objectives opened up the possibility of objective-based TIRHM. The use of objectives improved spatial resolution, and TIRHM is used to quantitatively characterize cell adhesion to petri surface [48–50] . TIRHM also obtains super resolved images with an in-line configuration and synthetic aperture approach [51]. However, matching amplitude and phase for obtained fields to create a super-resolved field becomes trivial when an off-axis configuration is used for hologram capture.

In this study, an objective based TIRHM system is realized. The system's design allows the apperture synthesis to further improve the spatial resolution. The system holds the potential for simplification and multimodal imaging [52,53]. We have demonstrated our system's capabilities by imaging microspheres with a diameter smaller than the diffraction limit, liquid interface, and living osteosarcoma (U2OS) cell extensions. Results show the potential strength of our method in studying cellular interfaces and other applications.

2.2. Experimental Setup

The main goal of this project is to image cell extensions with high resolution. The general experimental setup is designed in a similar fashion to an inverted microscope to make it easier to work with cell culture samples. An objective-based TIR configuration is realized in this experimental setup to satisfy the resolution condition. The incoming beam to the objective is focused on the back focal plane of the objective (BFP) to create a uniform bright-field illumination in the sample plane. The incidence angle for illumination can be controlled by changing the focus position of incoming light in BFP. If the beam is closer to the sides of the objective, the incidence angle gets larger. To control position of the beam in BFP, a mirror is placed into the focal plane of the tube lens (TL). The overall schematic of the experimental setup can be seen in Figure 2.1.

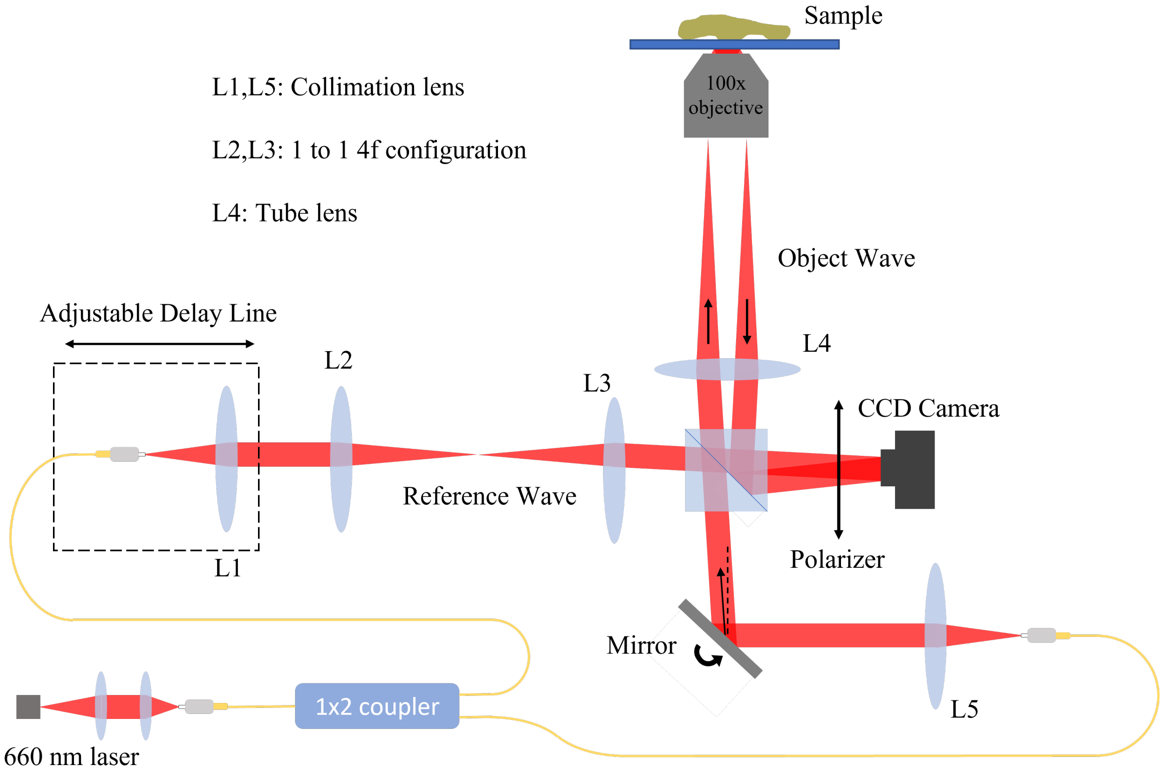

Figure 2.1. Schematic for built TIRHM experimental setup.

For illumination, light coming from 660 nm laser diode is first collimated and then coupled in to a single mode fiber. After light passes through a 1x2 coupler, one of the coupler outputs is used for creating illumination in reference arm whereas the other output is used for creating illumination in object arm.

In Figure 2.1, the mirror controls the position of the incoming beam on the tube lens. Since the mirror is placed in the focal plane of the tube lens, the spatial shift on the tube lens is translated to the focal plane of the tube lens which coincides with the BFP of the objective. The objective (Zeiss α Plan-Fluar 100x/1.49) used in experiments has typically a tube lens with a focal distance of 165mm and 1″ diameter. However, a tilt in the mirror can create beam clipping effects in the tube lens if an illumination with 1″ is used. Using a broad illumination is desirable to get a uniform intensity in FoV on camera for more consistent performance. So to prevent beam clipping effects, a tube lens (Thorlabs ACT508-200-A-ML) with 2″ diameter and a focal length of 200mm is used. The use of a 200mm focal length tube lens increases the total magnification of the system to $M = 100 \cdot \frac{200}{165} = 121.21$.

The next significant limitation to the system comes from the off-axis angle for the reference beam, which is critical for preventing aliasing with zero-order term as described in the Section 1.1.3.2. The smallest resolvable distance on the camera for coherent illumination, including the magnification, can be expressed as

$$d_{smallest} = \frac{M \cdot \lambda}{NA}. \tag{2.1}$$

Here M denotes the system's magnification, λ is the wavelength of illumination, and NA is the numerical aperture of the objective or imaging lens. For an objective with 1.49 NA, illumination light with $660nm$ wavelength and a magnification of 121.21, this limit gives a spatial frequency of

$$\omega_b = \frac{2\pi}{d_{smallest}} = \frac{2\pi \cdot NA}{M \cdot \lambda} = 2\pi \cdot 18625m^{-1}. \tag{2.2}$$

For zero aliasing with different orders, modulation frequency for off-axis configuration should satisfy

$$2\pi \frac{\sin\theta}{\lambda} \geq 3\omega_b, \tag{2.3}$$

$$\theta \geq 2.11°. \tag{2.4}$$

We can find the maximum pixel size for the camera considering the exact fit in Fourier space as depicted in Figure 2.2. The size of the Fourier domain is decided by the pixel size of the camera Δx and equals to

$$\omega_{x,max} = \frac{2\pi}{2 \cdot \Delta x}.$$

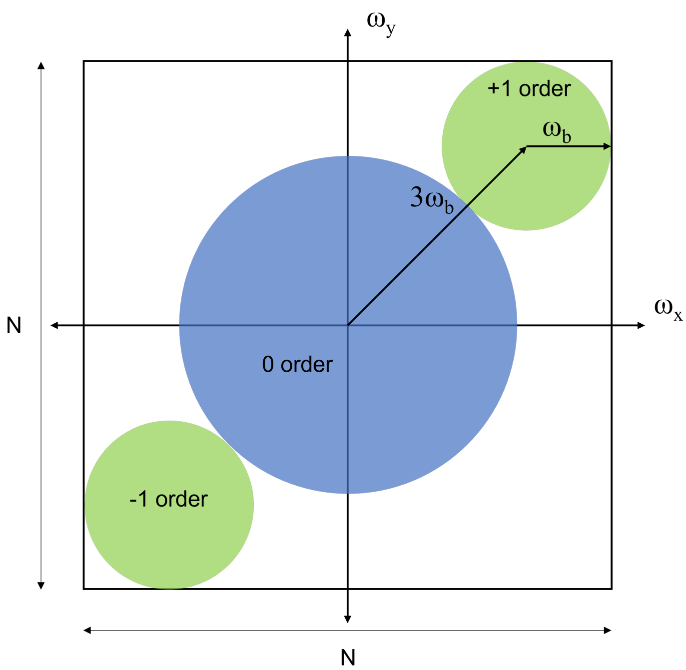

Figure 2.2. Ideal placement of interference orders in Fourier space for optimum bandwith usage.

If we consider an equal-sized pixel in x and y direction for the camera

$$\omega_{x,max} \geq \frac{3\omega_b}{\sqrt{2}} + \omega_b, \tag{2.5}$$

$$\Delta x \leq 17.2\mu m. \tag{2.6}$$

Most commonly used scientific cameras satisfy this pixel size condition.

To decrease aberration coming from possible curvature mismatch, L3 in Figure 2.1 is chosen to be the same as L4. For the reference beam, an incidence angle of 2.11 degrees can be created by sending the reference beam with a misalignment of $\tan(2.11°) \cdot 200 = 7.36mm$. This can be achieved by either controlling the position of the beam formed after L1 and L2 or by using a diffraction grating as shown in Figure 2.3.

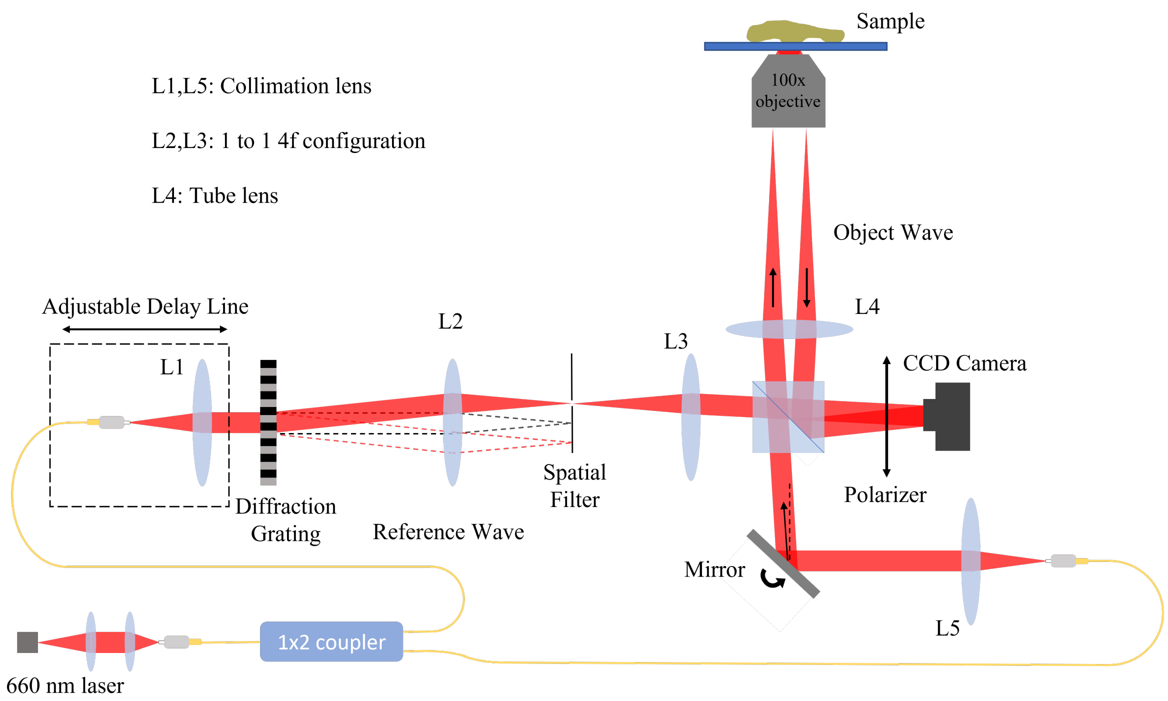

Figure 2.3. Schematic for built TIRHM experimental setup with grating in reference arm to reduce effect of temporal coherence.

The use of diffraction grating also reduces the system's temporal coherence noise, decreasing the hologram's phase noise and improving performance. Although the main problem in the initial development of holography was finding illumination sources with long coherence lengths, the effect of parasitic interference can be reduced by decreasing the coherence length of the illumination. However, lower coherence length means larger distribution in the spectral domain, which may cause chromatic aberrations in the optical setup. An additional spatial filter can be employed in the reference arm to block undesired diffraction orders and clean the reference beam. The spatial filtering of the reference beam becomes especially important if the diffraction grating is not perfectly clean, as it is virtually impossible to clean surface relief gratings without damaging the structure properly. Another problem coming from using a short coherence length illumination source is that the optical path lengths for the reference and the object arms should perfectly match to create an interference pattern on the camera. An adjustable delay line is employed for both experimental configurations in reference arm to achieve this. The design of the experimental setup is completed in CAD software. The CAD drawings for the reference arm and object arm can be seen in Figure 2.4 and Figure 2.5, respectively. The realized experimental setup can be seen in Figure 2.6.

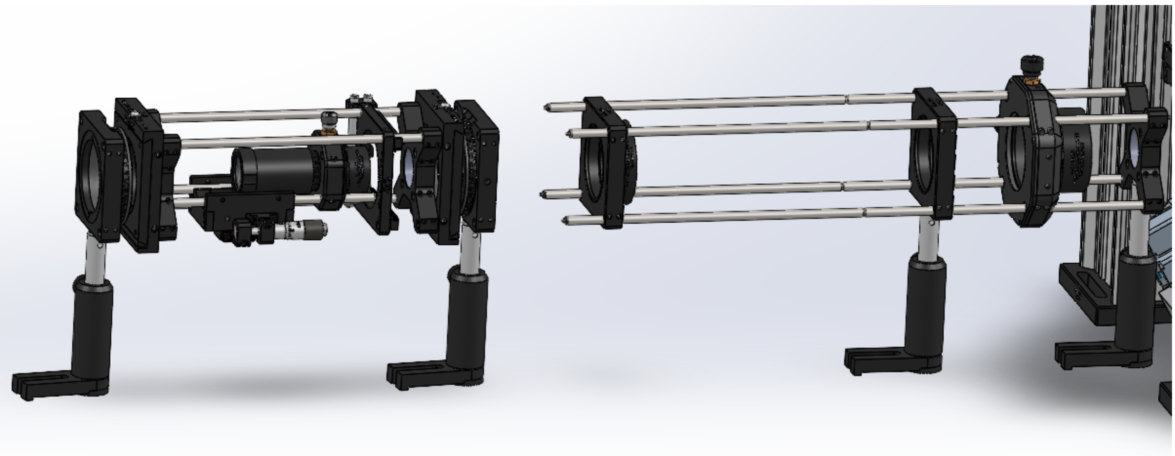

Figure 2.4. CAD drawing for the reference arm with diffraction grating.

2.3. Experimental Results

Experimental results are divided into three parts. The first group of results consists of phase images taken from flat surfaces for the system's phase noise and incidence angle characterization. Second results are taken with microspheres presenting the resolution limit of the system. Final results are taken from live-cell samples for the imaging of their extensions which was the primary goal of this study.

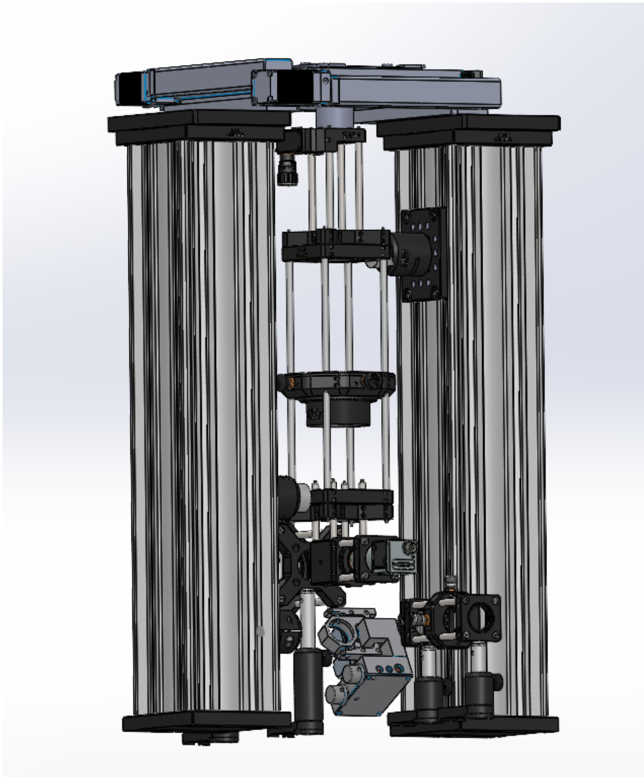

Figure 2.5. CAD drawing for the object arm and motorized stages.

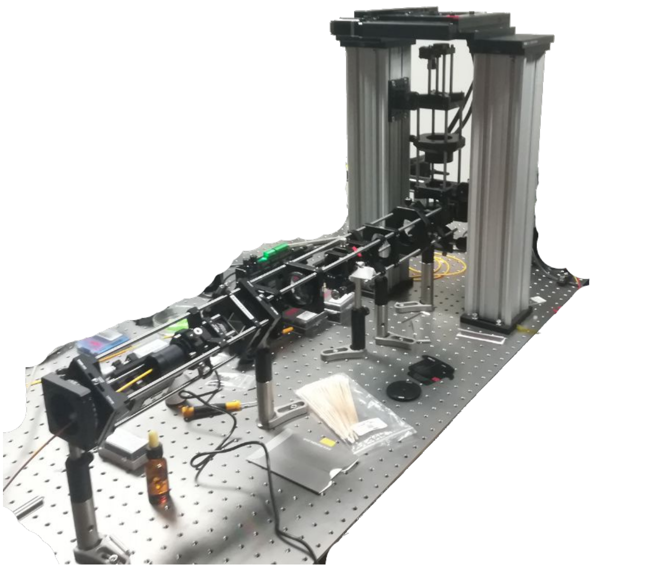

Figure 2.6. Image of built experimental setup.

2.3.1. Phase Reconstruction

The delay line for setup is optimized for maximum fringe visibility for hologram capture. An example of hologram and fringes can be seen in Figure 2.7.

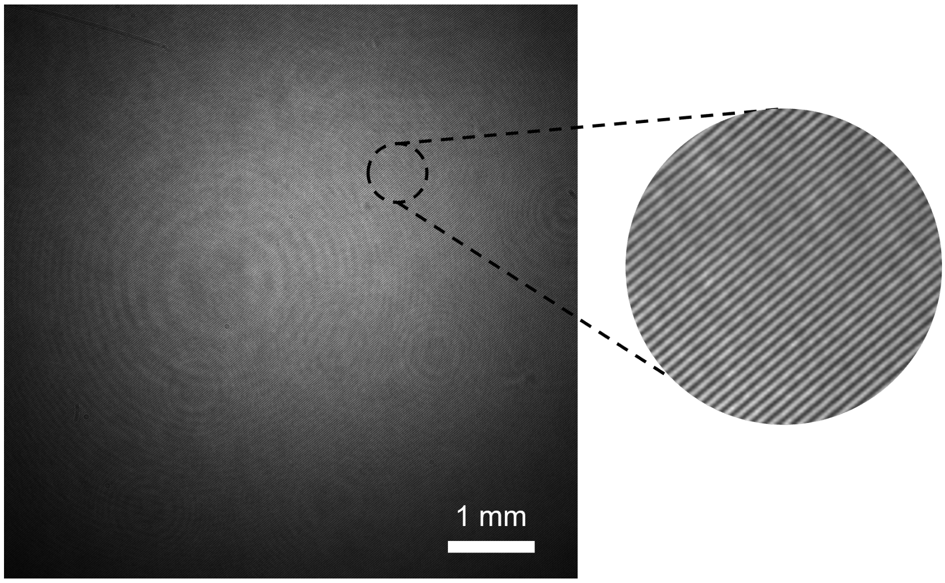

Figure 2.7. Interference pattern from obtained hologram to show fringe contrast.

A filter is applied to the Fourier transform of the hologram to isolate the cross-correlation terms as described in the Section 1.1.4. Figure 2.8 shows the absolute value of FFT of hologram in log scale. The blue circle indicates the border for the bandpass filter applied for Fourier filtering.

The phase curvature coming from curvature mismatch between reference and object wave and effect of linear phase terms is corrected by NPL by looking at the profiles where the sample is flat. The FFT of filtered NPL corrected hologram and phase obtained from this hologram can be seen in Figure 2.9a and b, respectively.

Alternatively, phase correction can be done using a reference hologram, as mentioned in the Section 1.1.4.2.

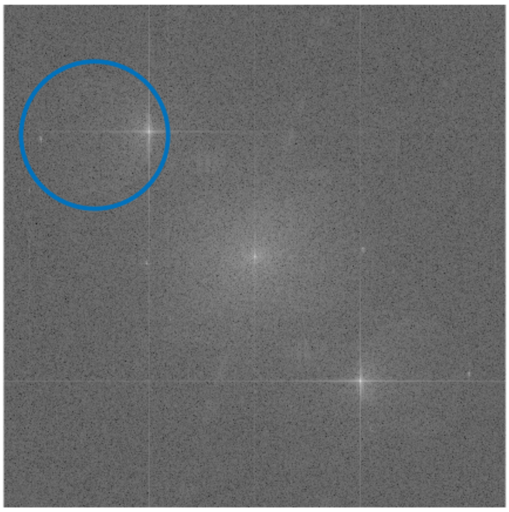

Figure 2.8. Filter (outlined by blue circle) applied in Fourier domain to reconstruct object wave.

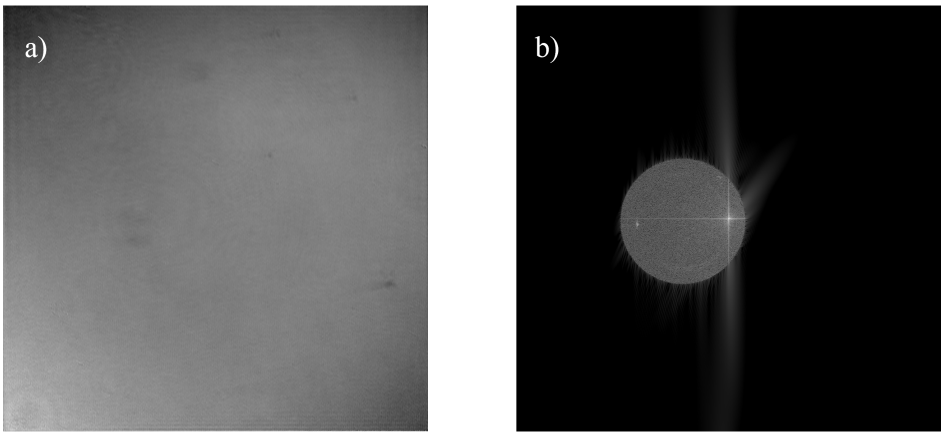

Figure 2.9. (a) Phase image obtained from NPL corrected complex field, (b) Fourier transform of NPL corrected complex field.

2.3.2. Flat Surface Results and Incidence Angle Characterization

Two main methods are mainly used in this project to measure incidence angle. The first method finds the location of maxima in the first-order term in Fourier space.

After the incoming beam interacts with the sample, some part of the beam gets scattered in every direction while the remaining part totally reflects with an angle equal to the incidence angle. If the initial illumination is uniform on the sample, Fourier transform or reflected beam is a Dirac delta function. This clear peak can be seen in Figure 2.9b. By measuring the distance between the center of the optically limited bandpass of the system and the position of Dirac delta, we can find the NA for the reflected beam, which can be turned to incidence angle by

$$NA_{incidence} = \frac{\Delta N_{incidence}}{\Delta N_{bandpass}} \cdot NA_{objective}, \tag{2.7}$$

$$\sin\theta_{incidence} = \frac{NA_{incidence}}{n_i}. \tag{2.8}$$

Here $\Delta N_{incidence}$ is the distance between the center of bandpass and Dirac delta in pixel, $\Delta N_{bandpass}$ is the radius of the bandpass of the optically limited system in pixel, $NA_{objective}$ is the numerical aperture of the objective and is the refractive index for immersion oil. The bandpass for the optically limiting system can be experimentally found by considering two opposing illumination directions with an illumination angle just above the critical angle for the system. The Fourier transform for these two cases is given in Figure 2.10. The Black dashed circle in this figure represents a slightly bigger bandpass for a system for viewing purposes.

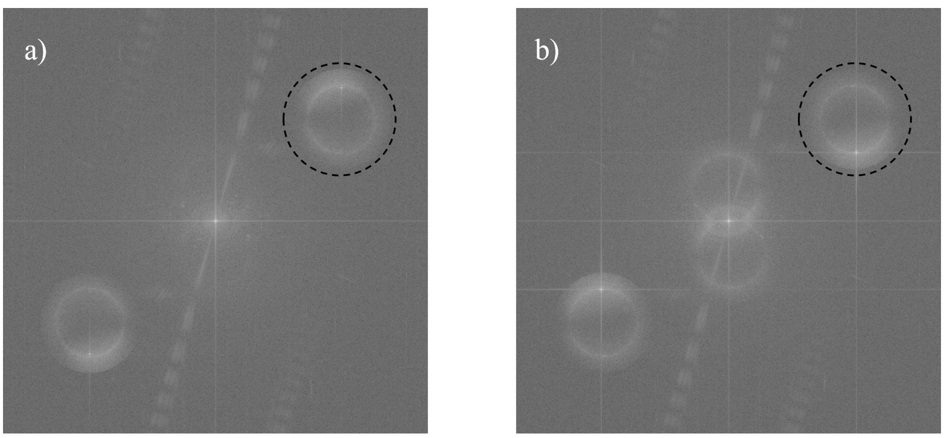

Figure 2.10. Fourier transform of obtained holograms which show the bandlimit for optically limited system for two different illumination angles.

Although this method is straightforward to implement, the accuracy is lower because of the low sampling capability in the Fourier domain. For built experimental setup, angle accuracy is around $\pm 1°$ for incidence angles around $60°$.

The second method for angle characterization utilizes the phase difference between two TIR waves. If there are two media with known refractive index in the FoV of the system, one can measure the phase difference between two reflected waves as shown in Figure 2.11.

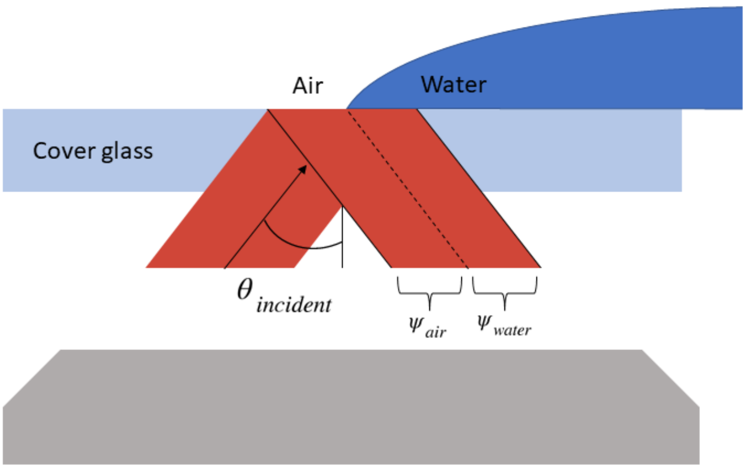

Figure 2.11. Schematic for TIR wave from glass-water and glass-air interface for incidence angle characterization.

The theoretical phase difference can be calculated from Fresnel coefficients for reflection and depends on the incidence angle and polarization as depicted in Figure 2.12a. Polarization can be selected for incidence angle calculation.

The amplitude and phase image from the water-air border with a profile along the blue line in the phase image is shown in Figure 2.13. The amplitude for totally reflected waves coming from the water and air region is nearly the same as shown in Figure 2.13a. This is because reflection coefficients R are equal to one since they are in TIR condition. However, the phase obtained from reflection for the two regions is considerably different. For this specific case, the phase difference between two regions is equal to 76.82° with a phase noise of 6.57°, which corresponds to an incidence angle of 62.16° ± 0.46°, which is more precise compared to the previous method and can further be improved using a p polarized beam.

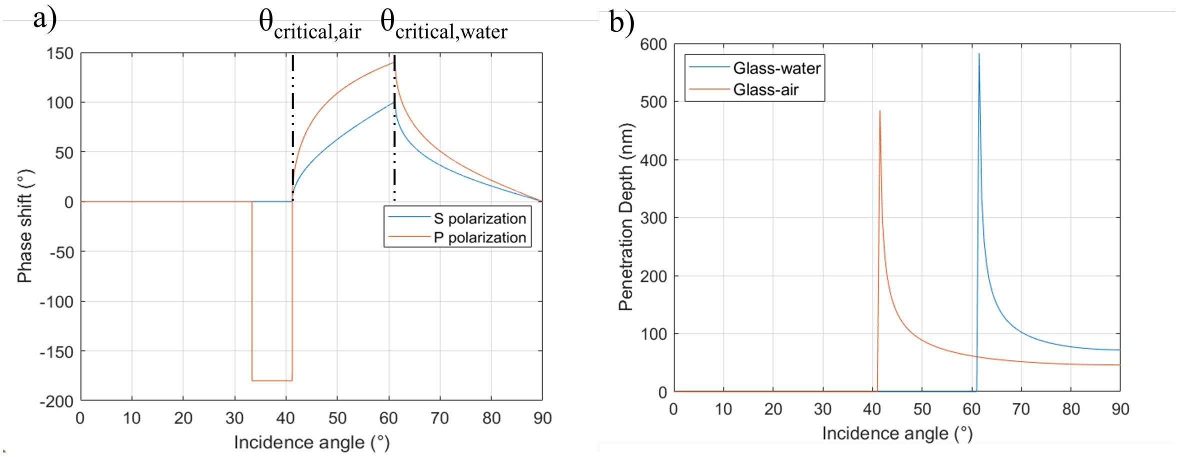

Figure 2.12. (a) Phase difference for TIR wave from glass-water and glass-air interface calculated from Fresnel Coefficients of reflection, (b) Penetration depth for evanescent wave in glass-water and glass-air interface for a light with 660 nm wavelength.

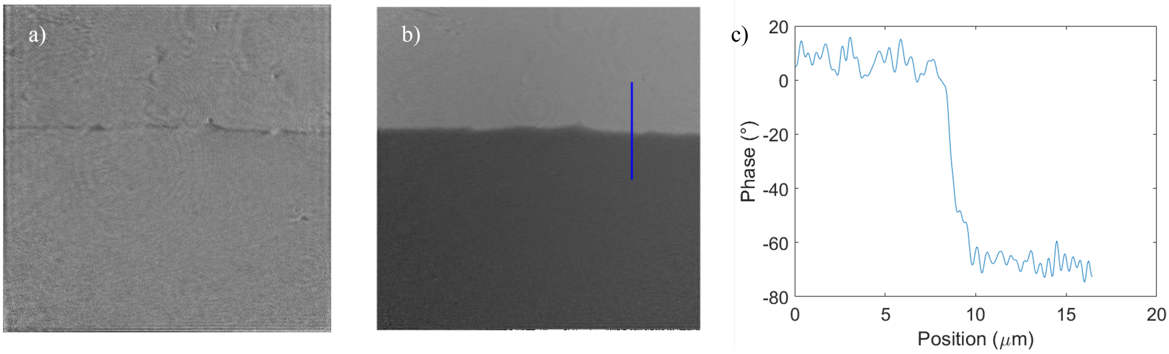

Figure 2.13. (a) Amplitude image, (b) Phase image obtained from water-air border as depicted in Figure 2.11, (c) Phase profile along the blue line for water-air border.

With known incidence angle, phase difference value can also be used to determine refractive index change. Plots for phase difference for an object with changing refractive index immersed in water are given in Figure 2.14. Here Figure 2.14a shows the TE (s) polarization case, whereas Figure 2.14b shows the TM (p) polarization. Among these θ values, 62.26° corresponds to slightly above of critical angle for glass-water, and 77.15° corresponds to slightly below the acceptance angle for the objective. The flat region for these graphs shows where the TIR condition is not satisfied for immersed object. For these graphs, refractive index of water and glass is assumed to be 1.331 and 1.518.

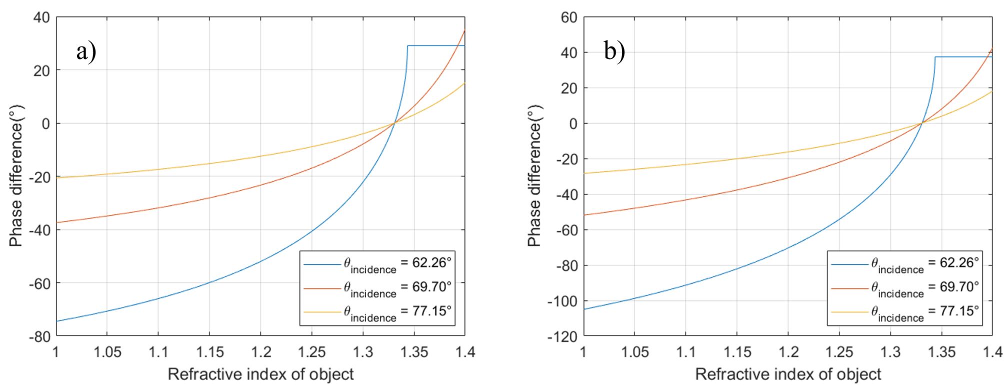

Figure 2.14. Phase difference between waves TIR from and object immersed in homogeneous medium for three different incidence angle for (a) s and (b) p polarizations.

From Figure 2.14, one can argue that the smaller incidence angles are always preferable compared to larger incidence angles because the phase difference obtained from reflection is larger for smaller incidence angles in most cases. However, from Figure 2.12b, it can be seen that the lower incidence angle corresponds to larger penetration depths. So the value of incidence angle should be optimized depending on application, considering penetration depth and phase difference.

2.3.3. Resolution Characterization

The minimum resolvable feature size on an optical system depends on the wavelength of the light used and the numerical aperture of the objective. For coherent illumination, minimum resolvable distance can be expressed as

$$d_{coherent} = \frac{\lambda}{NA} = 442nm.$$

For our experimental case, the wavelength of light is 660 nm, and the NA of the objective is 1.49. The Abbe resolution limit of the same case can be found by

$$d_{incoherent} = \frac{\lambda}{2 \cdot NA} = 221nm.$$

Which corresponds to an incoherent illumination case. Since these distances are smaller than even group nine element six of standard USAF resolution targets, resolution tests are completed using microspheres with known diameters. Microspheres are diluted in a 1:1000 ratio with distilled water, and a droplet is placed on the coverglass for sample preparation. During the evaporation of the distilled water, the surface tension of water brings microspheres closer, so pairs of microspheres can be found easily after the remaining water evaporates completely. For the resolution experiments, polystyrene microspheres with a diameter of 465 nm, 380 nm, and 300 nm are selected. 465 nm corresponds to the case where the distance between spheres is slightly bigger than $d_{coherent}$, whereas 380 nm and 300 nm case corresponds to point where distance is below the $d_{coherent}$ but above the $d_{incoherent}$.

<u>2.3.3.1. 465nm Diameter Microspheres.</u> Experimental results obtained from 465 nm diameter microspheres are shown in Figure 2.15. Figure 2.15a shows the bright field image of the microspheres to verify their positions, Figure 2.15b and c show amplitude and phase images reconstructed from the hologram, and Figure 2.15d) shows the amplitude and phase profiles along a microsphere pair. Two clear, distinct peaks verify that this setup's resolution is better than 465 nm, as expected.

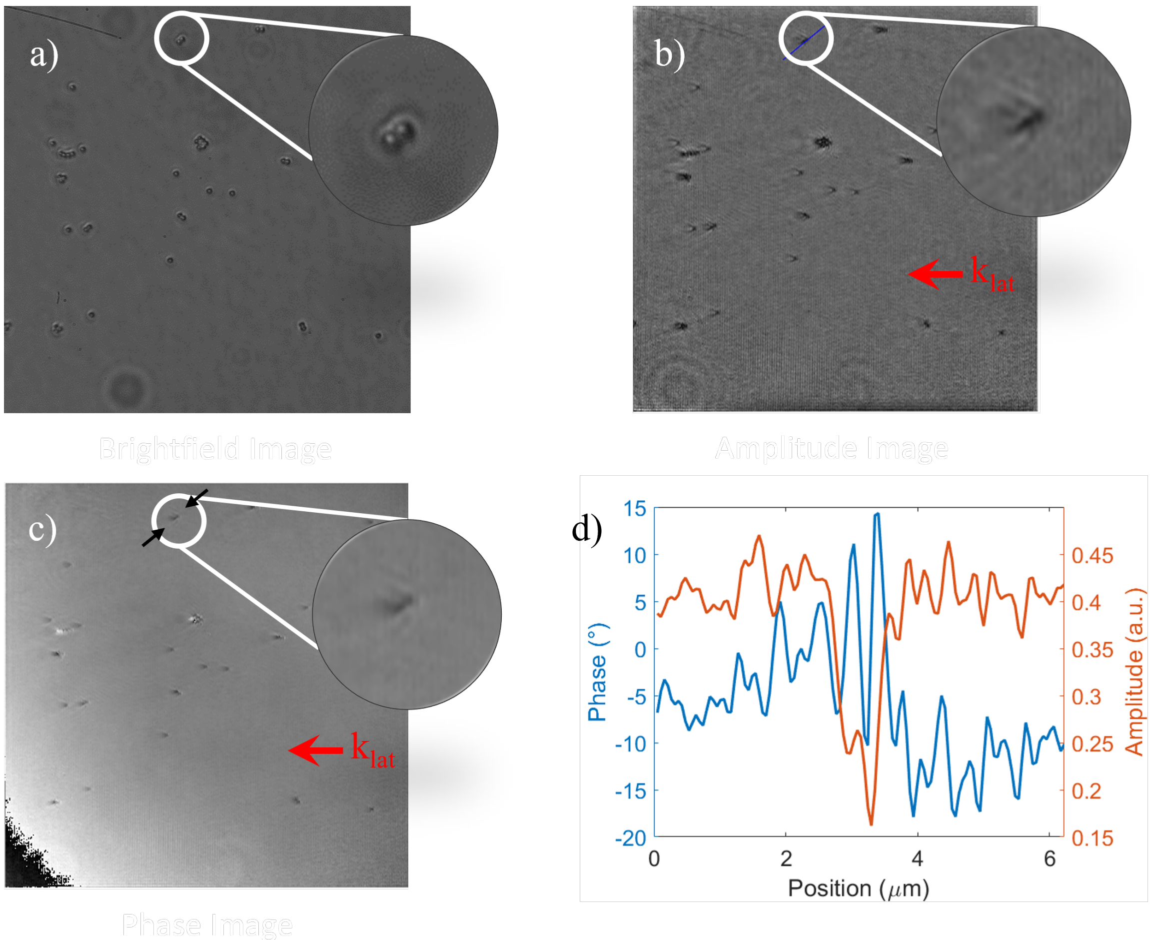

Figure 2.15. (a) Bright-field image showing microsphere doublet (b) Amplitude image (c) Phase image (d) Amplitude and phase profiles along microsphere doublet.

If we look more closely at the phase profile, we can see that the left side of the double peak has a higher value than the right side. This is because the collected light is not symmetric in the Fourier plane as we can see from Figure 2.9b. This asymmetry results in a preferred direction for light and creates ripples in the lateral direction for wave vector (k) of incoming light. Asymmetry can be tackled by illuminating the sample from two opposite directions to create a symmetric image in Fourier space. This approach of combining two illuminations with opposite directions also improves resolution beyond the limit for coherence illumination. This method is called as the aperture synthesis [54, 55].

Usually, one should be careful while combining complex fields from two illuminations because the k vectors are on spherical surfaces in 3D k space [56]. However, the limited penetration depth of evanescent waves restricts the possible k vectors to a 2D plane, so it is possible to directly add the complex fields for resolution improvement.

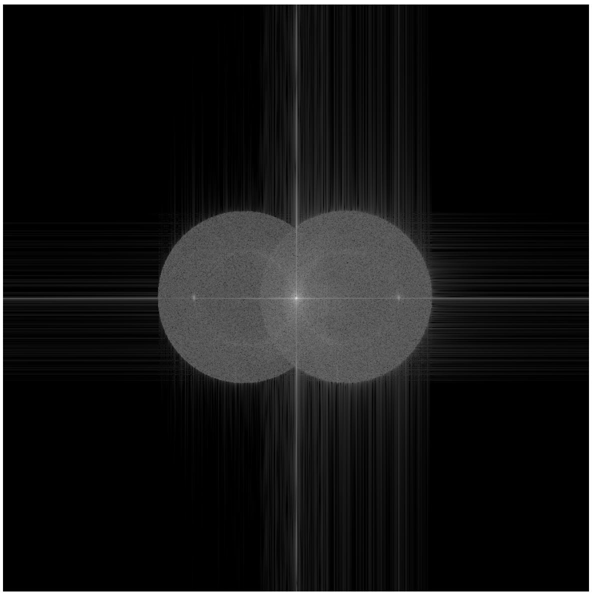

Figure 2.16. FFT of complex field obtained by combination of two opposite illuminations.

The FFT of the final complex field obtained from two illuminations with opposite directions and the same incidence angle magnitude is shown in Figure 2.16. An increase in the bandwidth of complex field improves the minimum resolvable distance by the system by

$$d_{c,synthetic} = \frac{\lambda}{NA_{objective} + NA_{illumination}}.$$

Here $NA_{objective}$ is the numerical aperture for the objective and $NA_{illumination}$ is the numerical aperture corresponding to the incidence angle for the illumination beam. Since

$$NA_{illumination} \leq NA_{objective},$$

the resolution obtained from synthetic aperture can reach up to Abbe limit in best case,

$$d_{c,synthetic} \geq d_{incoherent}.$$

The performance of the synthetic aperture approach has been verified by obtaining and combining holograms in opposite illumination directions. The results are shown in Figure 2.17. The Figure 2.17a shows the bright field image of a microsphere couple, Figure 2.17b and c shows the profile obtained from combined phase and amplitude images, respectively. Figure 2.17d and e show phase images obtained from single sided illumination, and the lateral vector belonging to illumination is given by the red arrow. Figure 2.17g and h show amplitude images obtained from single sided illumination, and again the lateral vector belonging to illumination is given by the red arrow. Figure 2.17f and i show the combined phase and amplitude images, respectively.

The effect of synthetic aperture and illumination direction can be seen more clearly in the closeup phase, and amplitude images belong to this FoV as shown in Figure 2.18. Figure 2.18a,h and o shows bright field images of microsphere pairs. Figure 2.18b,c,i,j,p and q shows phase images obtained by illumination from single direction. Similarly Figure 2.18e,f,l,m,s and t shows amplitude images obtained by illumination from single direction. Figure 2.18d,k and r shows combined phase images. Figure 2.18g,n and u shows combined amplitude images.

In Figure 2.18b, one can see the tails of the comet shape, which is caused by the lateral k vector belonging to illumination. The reversing of illumination direction changes the direction of the comet shape. When two illumination angles are combined, peaks in phase images get more isolated, as shown in Figure 2.18d,k and f. These experiments are repeated in two different fields of view to remove any suspicion from the reader.

The mean for phase and amplitude profiles obtained from nine microsphere pairs are given in Figure 2.19. In Figure 2.19, the highlighted area shows the standard deviation, whereas the bold line shows the mean value.

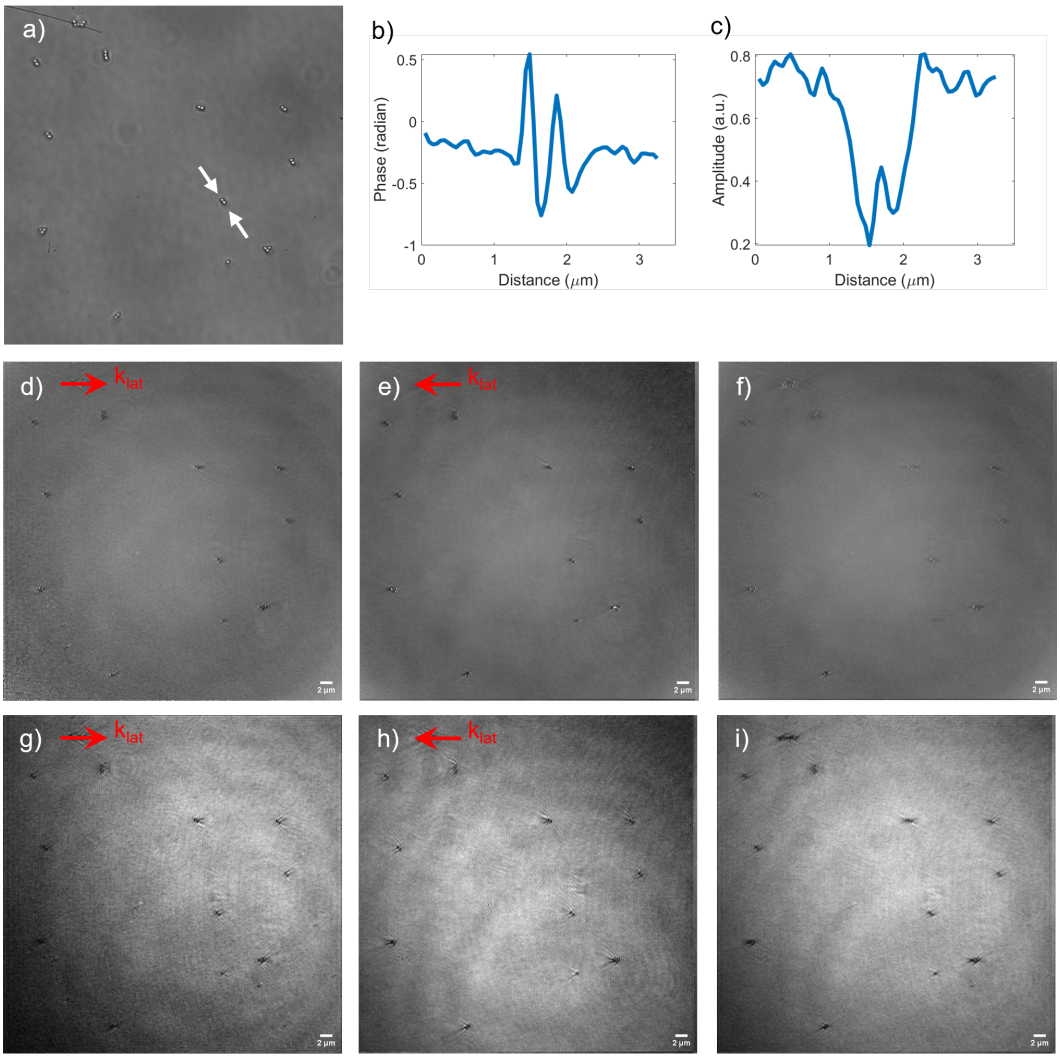

Figure 2.17. Obtained bright-field, phase and amplitude images for 465 nm diameter microspheres.

<u>2.3.3.2. 380 nm Diameter Microspheres.</u> For microspheres with 380 nm diameter, the same experimental procedure as explained in the chapter is followed. Results can be seen in Figure A.1, A.2, and 2.21. Two clear peaks in amplitude and phase images as shown in Figure 2.21a and b confirms that the resolution of system is indeed enough to resolve 380 nm features. So the application of synthetic aperture improves the resolution of the system as expected.

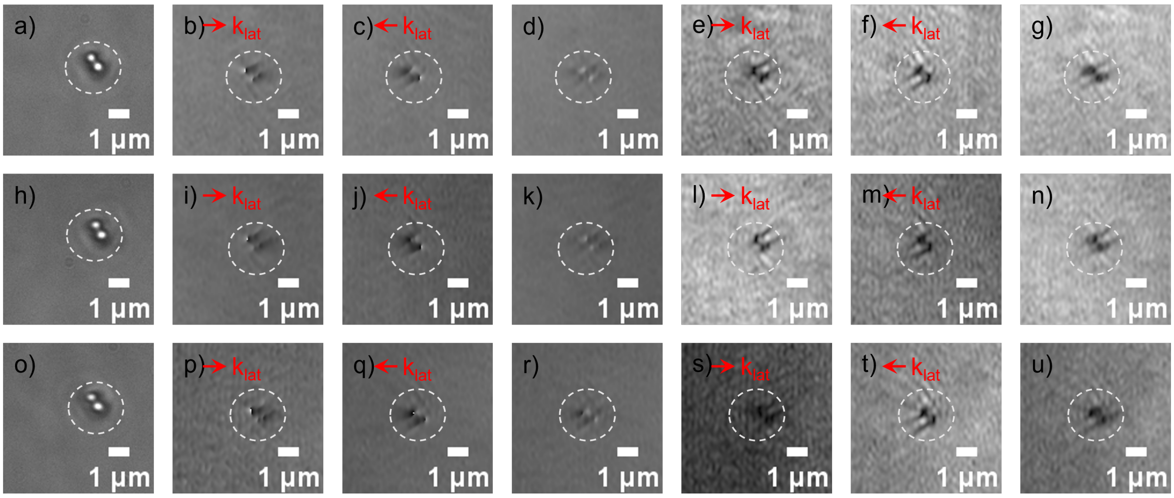

Figure 2.18. Closeup of obtained bright-field, phase and amplitude images for 465 nm diameter microspheres.

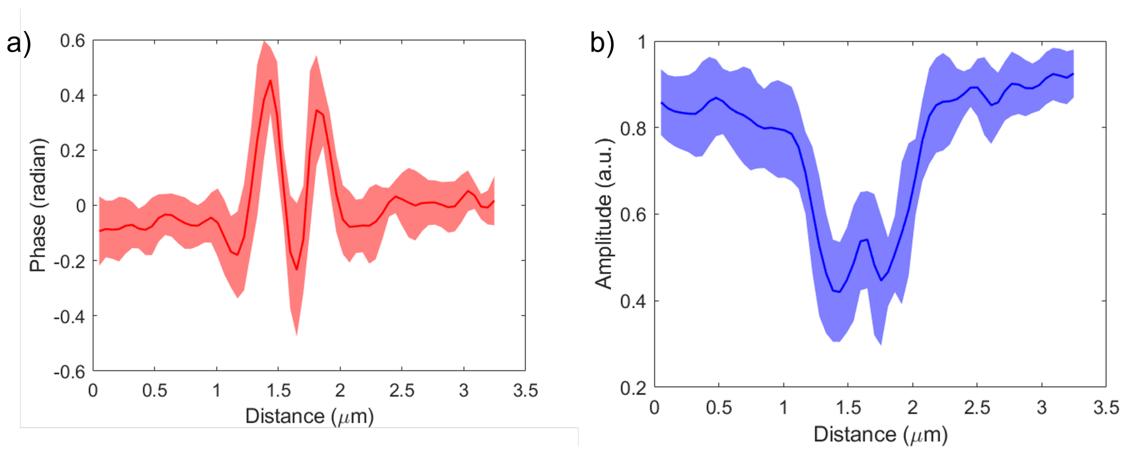

Figure 2.19. (a) Mean phase profile, (b) Mean amplitude profile obtained from nine different microsphere pair for 465 nm.

<u>2.3.3.3. 300nm Diameter Microspheres.</u> For the final set of results for resolution characterization, microspheres with 300 nm are imaged and results are shown in Figure A.3, A.4, and 2.20. Two distinct peaks in amplitude and phase images as shown in Figure 2.20a and b, confirms that the resolution of system is indeed enough to resolve 300 nm features. The precise experimental resolution of system can be found by using a radial resolution target in which the distance between two adjacent feature is chang-

ing continuously with radial distance. However, production of these radial resolution targets are not trivial for hundred nm order and require clean room to fabricate. So, the resolution of system is verified to be better than 300 nm but exact experimental value is unknown.

2.3.4. Preliminary Live Cell Results

For the final set of results, live U2OS cells are imaged with TIRHM setup. This adherent cell line is derived from human bone osteosarcoma epithelial cells and has been in the interest of mechanobiology studies due to its dynamic and thick cytoskeletal components on the cell membrane [57, 58]. Preliminary results showing amplitude and phase images of two different cells can be seen in Figure 2.22. By setting a limit on phase change, the area of cell which is in contact with glass can be quantitatively measured.

In Figure 2.22a and c, the areas where cell is in contact with glass has lower intensity compared to background. This means that the light is frustrated and the incidence angle is not optimal, a higher value for incidence angle should be used. Also illumination is not completely homogeneous in FoV. This can be corrected by using a bigger beam waist for initial beam after collimation. However, in phase images contact area has a different phase value compared to background which can be used to quantify contact area as expected. Although these are preliminary results, it shows the potential of current configuration.

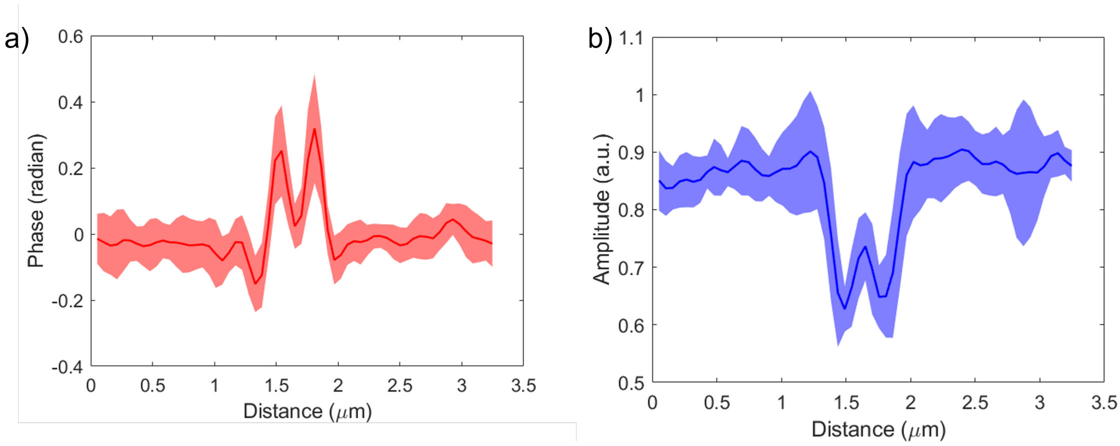

Figure 2.20. (a) Mean phase profile, (b) Mean amplitude profile obtained from nine different microsphere pair for 300 nm.

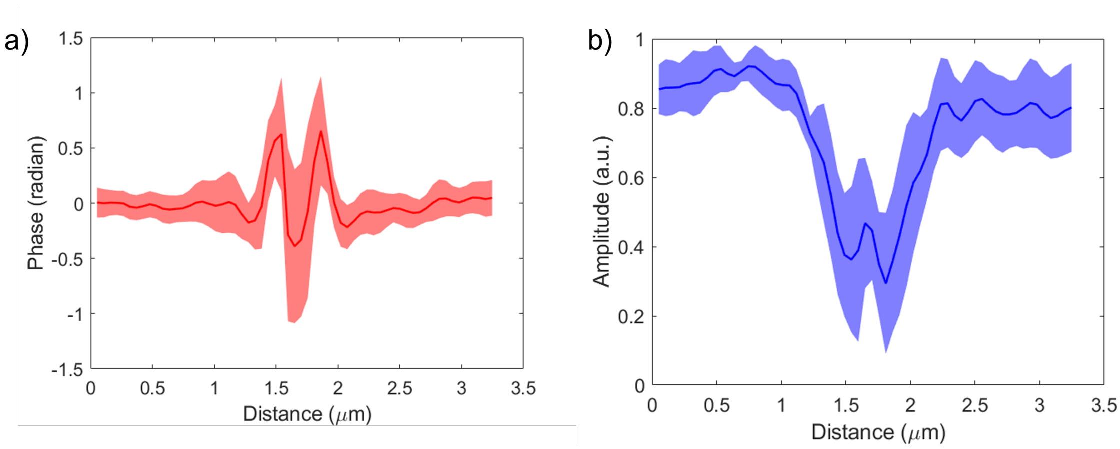

Figure 2.21. (a) Mean phase profile, (b) Mean amplitude profile obtained from nine different microsphere pair for 380 nm.

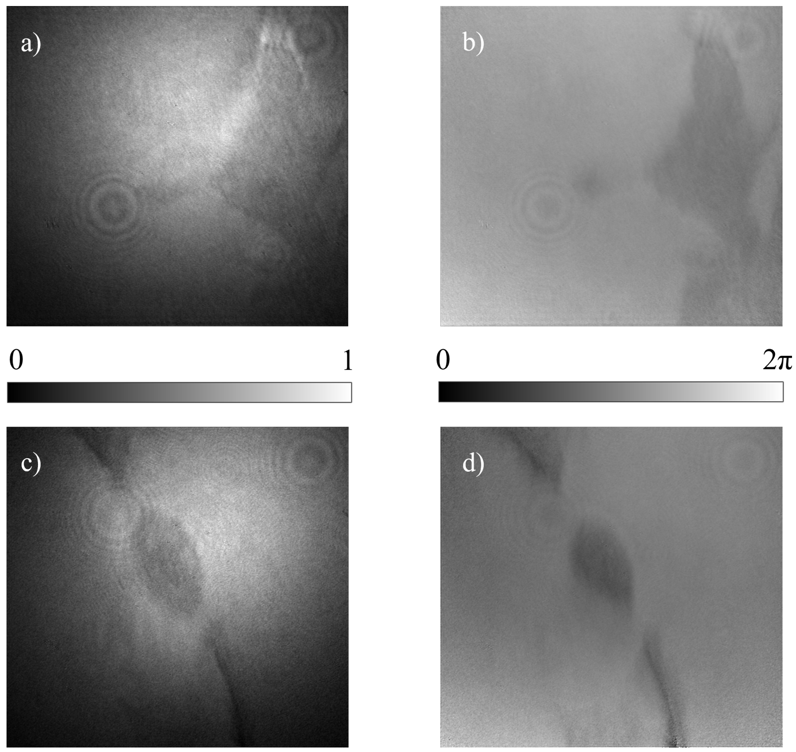

Figure 2.22. (a,c) Amplitude image of U2OS cells, (b,d) Phase Images of U2OS cells.

3. MASKLESS LITHOGRAPHY WITH HOLOGRAPHIC FEEDBACK

3.1. Fabrication of Micro-optical Elements

Up until now, the focus of this thesis was to highlight the capabilities of the developed TIRHM setup. However, alternative imaging methods are available for phase imaging, such as Zernike phase contrast microscopy, which requires a specific phase plate. Also, other super-resolution approaches such as stimulated emission depletion microscopy (STED), require a phase plate to create depletion illumination [59]. Although spatial light modulators (SLM) are widely used to control the phase of light, they are generally an overkill to create non-changin phase retardation on the wavefront as high-resolution SLMs are expensive and remain as bulky solutions where size is a constraint for the system. Grayscale lithography is a well-known method for the production of phase plates [60]. However, the lack of closed-loop control in lithography applications decreases performance and increases the susceptibility of the lithography systems to environmental changes. Also, for every photoresist, a calibration should be done to characterize the response of photoresist to illumination to create a structure with desired height. These requirements increase the cost and decrease the availability of lithography setups to scientific community. This chapter introduces a new closed-loop control algorithm for maskless lithography setups that utilize quantitative phase imaging capabilities of digital holography.

3.2. Lithography

Lithography is the general term used for transferring the desired pattern on a photosensitive substrate. The exposed substrate can then be developed by chemical treatment to get the desired shape. Lithography can be divided into two parts by transferring geometry. Proximity lithography utilizes a physical mask to block the illumination light, which induces chemical changes in the photosensitive substrate as shown in Figure 3.1. In this configuration, the distance between mask and substrate is as small as possible to reduce effects coming from the propagation of diffracted light.

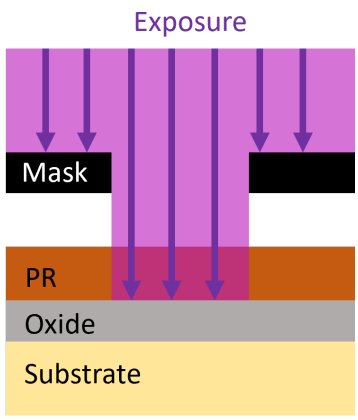

Figure 3.1. Schematic for proximity lithography.

The second configuration utilizes an imaging setup to image a physical mask on to the substrate. In this configuration, the performance of lithography dramatically depends on the quality of the imaging setup. However, the physical mask can be interchanged by SLMs or light projectors to create the mask dynamically. This reduces the cost of mask fabrication and ultimately enables the prototyping for lithography applications.

Traditionally, lithography either completely cures or does not cure the photoresist. After the developing process, the end product has a 'binary' height distribution across the sample. Although this might be desired in some cases, like in semiconductor manufacturing, there is a need for structures whose height changes continuously like in a lens. By changing the light dose, one can obtain 3D structures, and this method is called as grayscale lithography.

Generally, for binary lithography, high contrast photo resists are preferred. The high contrast means that the depth of substrate after developing process changes quickly with exposure does as shown in Figure 3.2. Low contrast photoresist is preferred for grayscale applications as it eases the requirements for exposure dose control.

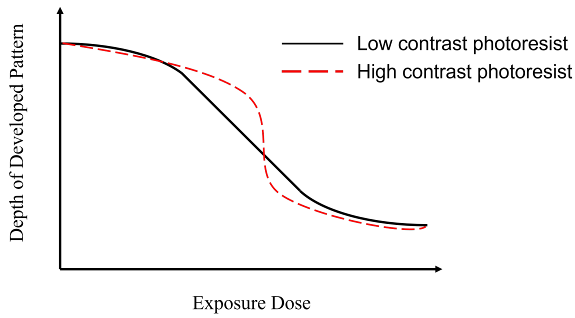

Figure 3.2. Etched depth vs exposure dose for low contrast and high contrast photoresist.

Maskless grayscale lithography can be used to create a variety of structures such as microfluidic channels [61], lenses [62], and gratings [63]. However, the efficiency of these devices depends heavily on printing quality which requires tight dimensional control. Tight production tolerances for feature size, height, and growth or etching rate require a pre-calibration run on a dummy wafer or sample. This process is repeated until error margins fall below the desired tolerances. Also, once the calibration is completed, the environmental conditions should not change not to affect the system as the system is inherently susceptible to environmental effects. Variations due to system drift cannot be corrected until too late because there is no feedback mechanism to correct and detect it in situ. An accurate, non-destructive, real-time in situ monitoring is highly desirable for correcting the change in processing conditions as it will enable feedback control of the system.

There are various optical characterization techniques, such as spectroscopic ellipsometry [64], phase-sensitive ellipsometry [65], laser reflectometry [66], multi-beam interferometry [67], and emission spectroscopy [68] which check the requirement for nondestructive testing but is generally used for single-point measurements. These techniques might be adequate for planar shapes but are insufficient in providing necessary feedback information to produce complex phase plates. An imaging method rather than a single point method is preferred to fully correct any deviation in the field of view. For this job, quantitative phase imaging stands out with its good performance in noisy environments. The phase of the sample can be obtained by the reconstruction of digitally recorded holograms in digital holographic microscopy (DHM) [14] or by various quantitative phase microscopy methods [52, 69, 70]. There are some preliminary works which utilize real-time quantitative phase imaging, but their use is mainly limited to the characterization of etching rates [71].

3.3. Feedback Loop

Here we propose an alternative to grayscale lithography, which utilizes phase imaging as feedback to improve printing quality. Our technique relies on the phase retardance measurements coming from the digital holography part of the setup to measure how phase of each point evolves in time and correct any deviations. Instead of using a long during single shot exposure to create the desired pattern, we divide the single shot into multiple shorter exposures to increase number of measurements. Between each exposure, the current phase of the sample is measured and from this, the difference to the target phase is calculated for each point. The input image for grayscale lithography is then adjusted according to this phase difference. Since this technique adjusts the light intensity in each step, precalibration of photoresist is not required.

To test the hypothesis, an experimental setup which is a simple combination of a maskless lithography and DHM is constructed. The general schematic of setup can be seen in Figure 3.3. Our proposed system uses the hologram captured by the camera to measure the optical phase map of sample at each step and apply required correction by changing the pattern projected on SLM.

The digital holography part of the system utilizes an off-axis configuration to create the hologram. The light coming from a 660 nm diode is divided into two by a beam splitter after spatial filtering. The light in object arm first passes through a delay line that is constructed by two right angle prism to match the optical path length of reference arm to create interference pattern. Then light in object arm passes through the sample and is imaged on camera by a unity magnification 4f imaging system. The collimated light in the reference arm is just reflected from mirrors to arrive at the camera. Light in the object and reference arm is brought together by a second beam splitter. The off-axis angle between reference and object arm can be adjusted by placing the second beam splitter by a slight tilt angle. The object beam reflecting from second beam splitter propagates in off-axis to create interference pattern on the camera. Once hologram is captured, Fourier filtering can be applied to find quantitative phase as explained in Section 1.1.4. Then a least square phase estimation method [72] is used to find the total final phase.

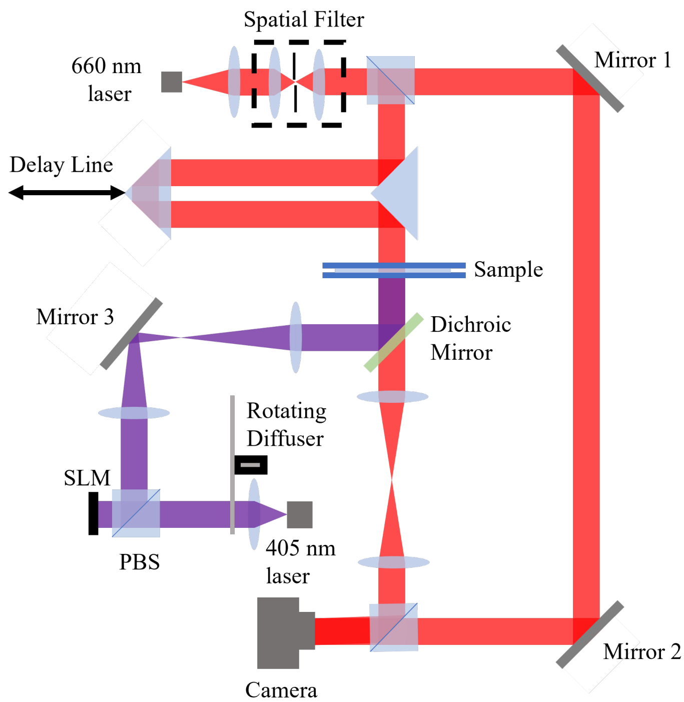

Figure 3.3. Schematic for maskless lithography setup with DHM capabilities.

For the grayscale lithography part, an SLM is illuminated by a 405 nm violet laser beam. The size of the beam is adjusted such that it overfills the SLM. The SLM is then placed on to the object plane of a 1 to 1 magnification 4f imaging system whereas sample is placed on the image plane. To reduce effect of speckles caused by the laser,a flat top diffuser (Thorlabs ED1-S20-MD) and a home made diffuser is mounted on a dc motor to act as a rotating diffuser is placed on the beam path. The SLM used in this experiment is taken out from a commercial projector (AAXA Technologies P3 Pico Projector) with 1024x600 native resolution and 9.45 μm pixel size(Syndiant Syl2061). Light reflected from SLM goes through a polarizing beam splitter to create contrast. For precise exposure times, the switching state of 405 nm laser is controlled by a L298N motor driver and Arduino. The fluence of near UV illumination on sample plane is $4.23\mu m/cm^2$.

Sample is prepared using OrmoComp® positive photoresist which is filled between two glass slides that seperated by a double-sided tape.

The light intensity on the sample plane is correlated to the image projected on SLM. By controlling the projected image, we can control the total light dose projected on a point and hence control the phase retardance of that point. This allows us to create any desired phase plate accurately without any prior calibration of the photoresist. However, photoresists require a threshold exposure dose before curing starts. This causes a problem for the system to reach lower phase targets and disrupts performance. A background of proper value ensures that the exposure dose is above the threshold value at every point in FoV. An example of addition of background to phase target can be seen in Figure 3.4

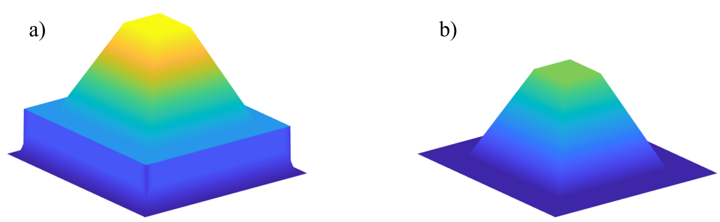

Figure 3.4. An example of a target phase with (a) added background, (b) without background.

A Gaussian filter of appropriate size can be applied to smooth out the edges of background to decrease phase unwrapping errors.

New pixel values for SLM are calculated using a linear approach. For pixel values 1-255, if the difference between the current and target phases is bigger than π, the pixel gets a value of 255. If the difference is smaller than π, new pixel value will be $\frac{\Delta\phi \cdot 255}{\pi}$.

Experimentally it is crucial to correctly map the pixels of SLM to the sample plane so an alignment run is required. For alignment, a binary phase target consisting of four crosshairs is written on the photoresist as shown in Figure 3.5. The centers of crosshairs are found in the phase image obtained from DHM. The projective transformation relating SLM pixels to the sample plane is then found by fitgeotrans() function in MATLAB.

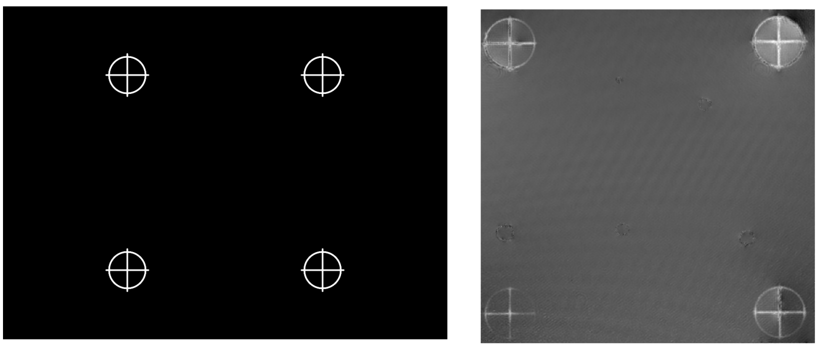

Figure 3.5. (a) Calibration target, (b) Resulting phase image.

For the break condition of the feedback loop, the average difference between the current and target phase is calculated. If the average falls below a particular threshold value, loop terminates. The overall flowchart of this method can be seen in Figure 3.6.

The exposure time is set to 50 ms for single illumination and generally after $\sim$ 125 iterations, loop breaks. Each iteration step takes $\sim$ 3 seconds, including phase reconstruction and unwrapping. The phase reconstruction, unwrapping and creation of new mask takes around two seconds. There is a one second wait after the new mask is produced to ensure renewed image is projected on SLM because an intermediary streaming program (OBS Studio) is used to project images. So total duration of fabrication is around seven minutes.

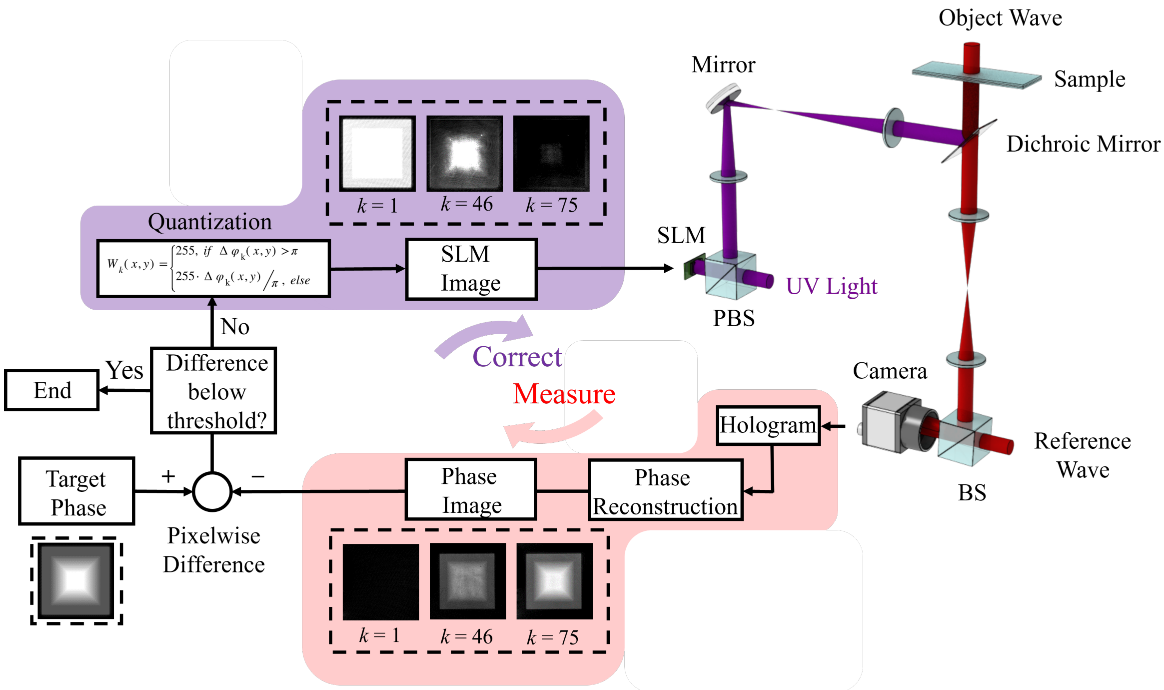

Figure 3.6. General flowchart for proposed method.

3.4. Results

To test the capabilities of the system, three different phase plates are fabricated. The first phase plate resembles a classical binary pattern with a square step in the middle. Phase retardation of the middle square and framing background is selected 3π and π, respectively. These values are decided considering the maximum phase retardation that the system can provide. Experimentally, the maximum value for phase retardation is found to be around 5π. This value significantly depends on the type of photoresist, the thickness of photoresist, and the depth of field of imaging optics. For the background value, a trivial value of π has been chosen as it performed well.

The resulting phase plates fabricated by the traditional single-shot method and proposed iterative method can be seen in Figure 3.7. Although the flatness of the top surface may be acceptable for the classical method, our approach improves this by also decreasing the standard deviation across the sample. The mean phase difference from the target for the classical and iterative cases are 0.44 and 0.26 radian, respectively.

The standard deviation from the target phase is calculated to be 0.1 and 0.05 radian for the classical and iterative methods, respectively. We can see that the iterative method provides immunity to nonhomogeneous UV illumination as the background and the top part has an increasing profile in the classical method. In contrast, it stays close to ideal for the iterative case.

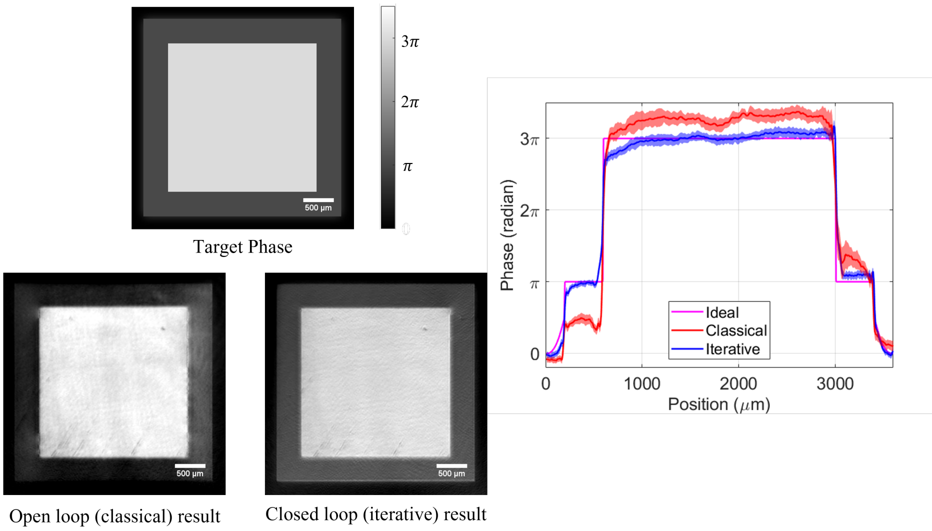

Figure 3.7. Experimental results obtained for 'binary' square phase target.

To test the system in constant slope scenarios, where grayscale lithography is mainly used, a pyramid shape with a flat area in the middle is chosen to be printed on photo-resist. The target phase for constant slope can be seen in Figure 3.4a. Results can be seen in Figure 3.8. For this case, the mean phase difference from the target for classical and iterative case are 0.82 and 0.18 radian, respectively. The standard deviation of phase for the iterative method is 0.06 radian and much smaller compared to the classical one with a standard deviation of 0.44 radian.

This result can be expected as grayscale applications generally require a calibration step to perform well. However, without any a priori calibration step, the iterative method gets the proper slope amount by constantly correcting deviations in the system. The effect of uneven illumination is also more pronounced here. The slope on the right and left sides for the classical result are not equal. So even though a precalibration step would ensure the correct slope for one side, it still does not correct nonhomogeneous illumination in the sample plane. This is again another powerful aspect of the iterative method.

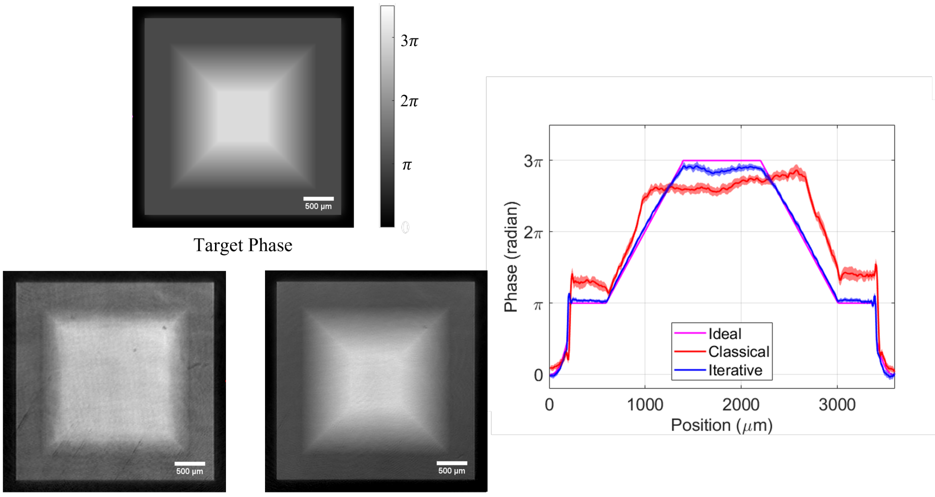

Figure 3.8. Experimental results obtained for constant slope phase target.

For final results, we considered a real use case, a spiral phase plate. Spiral phase plates are elements whose phase increases with azimuth angle. Depending on the interval of phase change $[0\ 2\pi l]$, it can also transfer angular momentum equal to $L = l\hbar$. Spiral phase plates are used to create doughnut-shaped depletion beams for STED applications, micromanipulation of trapped particles, and in phase-contrast microscopy [73]. Results can be seen in Figure 3.9.

Since DHM gives the full complex field, the beam which forms after passing through the phase plate can be numerically propagated. Results for numerical propagation and physical propagation are given in Figure 3.10. Numerical and physical propagation results agree with each other, and there is a clear dip in intensity at the center beam as expected.

To sum up, a new iterative method that utilizes the DHM to create a feedback loop for maskless lithography is realized. This presented method finds the current phase change of specimen near real-time nondestructively by utilizing a digital holographic imaging setup. Using the information about phase change, the method decides on the new intensity mask to be shown in SLM, which reduces both standard deviation and mean difference in the resulting phase plate. This system reduces the effect of homogenous UV intensity in the target plane, the nonlinearity of photoresist, etc., on the final phase distribution.

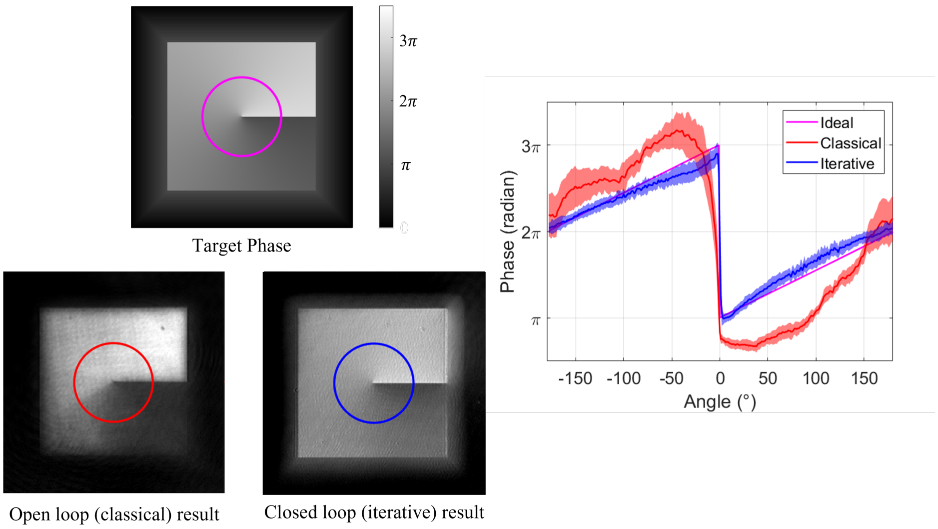

Figure 3.9. Experimental results obtained for spiral phase plate.

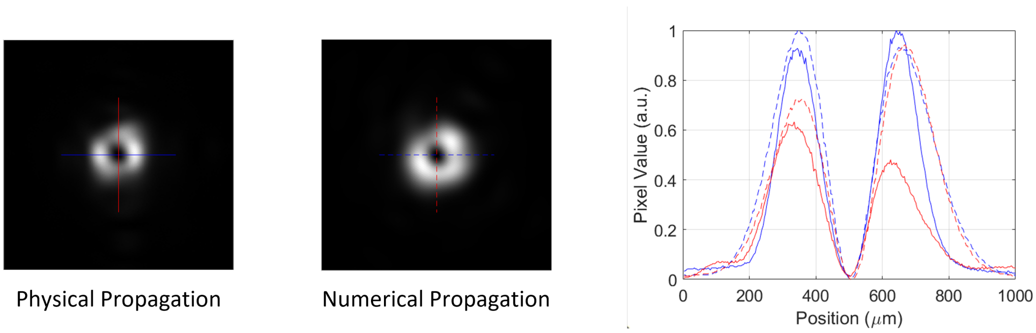

Figure 3.10. Results for physically and numerically propagated waves after passing through phase plate.

4. CONCLUSION

In this study, an off-axis digital holographic total internal reflection microscope is realized. Total internal reflection configuration removes the requirement for optical sectioning methods for examination of interface structure. The quantitative phase imaging capabilities of DH, enables characterization of surface topography of specimen unlike total internal reflection fluorescence microscopy which is the standard imaging modality for the investigation of interface structures.The incidence angle for beam can be measured by either using Fresnel coefficients or by examining the position of non-diffracted light in Fourier space. This enables fast and reliable calibration methods for refractive index mapping.

The incidence angle for illumination creates lateral propagation vectors on specimen which turns an image of a point to a comet like structure and creates different resolution distances depending on direction. Since the TIR is achieved by an objective in our setup,the direction of illumination and incidence angle is controllable. The complex fields obtained from different illumination directions can be synthesized following synthetic aperture approach to go beyond diffraction limit in resolution for every direction.

The improved resolution of system is verified by imaging microspheres with diameter of 465 nm, 380 nm and 300 nm. In all cases, the system is able to resolve two adjacent microspheres clearly. With characterized spatial resolution and incidence angle, cell adhesion experiments are performed. For cell imaging, U2OS Osteosarcoma cell line embedded in petri dish are imaged. The cell extensions and points of contact can be characterized quantitatively from obtained holograms.

Additionally a grayscale UV lithography method is developed where the pattern for grayscale is updated from phase measurements of specimen in real time. This allows for real time corrections for deviations caused by nonidealities embedded in the system. This method removes the requirement for calibration of photoresist and shown to be working well even in nonhomogeneous illumination of sample. A spiral phase plate, which has uses in differential contrast microscopy or STED microscopy, is fabricated by proposed method and shown to perform better compared to classical counterpart. Resulting doughnut beam shape, is imaged to verify effectiveness of proposed feedback method for micro-optic fabrication.

REFERENCES

1. Gabor, D., "A New Microscopic Principle", *Nature*, Vol. 161, No. 4098, p. 777–778, 1948.

2. Gabor, D. and W. L. Bragg, "Microscopy by Reconstructed Wave-fronts", *Proceedings of the Royal Society of London. Series A. Mathematical and Physical Sciences*, Vol. 197, No. 1051, pp. 454–487, 1949.

3. Gabor, D., "Microscopy by Reconstructed Wave Fronts: II", *Proceedings of the Physical Society. Section B*, Vol. 64, No. 6, pp. 449–469, 1951.

4. Denisyuk, Y. N., "Photographic Reconstruction of the Optical Properties of an Object in Its Own Scattered Radiation Field", *Soviet Physics Doklady*, Vol. 7, p. 543, 1962.

5. Stroke, G. W., "An Introduction to Coherent Optics and Holography", *New York: Academic Press*, 1966.

6. Goodman, J. W. and R. W. Lawrence, "Digital Image Formation From Electronically Detected Holograms", *Applied Physics Letters*, Vol. 11, No. 3, pp. 77–79, 1967.

7. Coquoz, O., R. Conde, F. Taleblou and C. Depeursinge, "Performances of Endoscopic Holography with a Multicore Optical Fiber", *Applied Optics*, Vol. 34, No. 31, pp. 7186–7193, 1995.

8. Coquoz, O., C. D. Depeursinge, R. Conde and E. B. de Haller, "Microendoscopic Holography with Flexible Fiber Bundle", *Clinical Applications of Modern Imaging Technology II*, Vol. 2132, pp. 466 – 474, 1994.

9. Schnars, U., "Direct Phase Determination in Hologram Interferometry With Use

of Digitally Recorded Holograms", *Journal of the Optical Society of America A*, Vol. 11, No. 7, pp. 2011–2015, 1994.

10. Schnars, U. and W. Jüptner, "Direct Recording of Holograms by a CCD Target and Numerical Reconstruction", *Applied Optics*, Vol. 33, No. 2, pp. 179–181, 1994.

11. Pedrini, G., Y. Zou and H. Tiziani, "Digital Double-pulsed Holographic Interferometry for Vibration Analysis", *Journal of Modern Optics*, Vol. 42, No. 2, pp. 367–374, 1995.

12. Pomarico, J., U. Schnars, H.-J. Hartmann and W. Jüptner, "Digital Recording and Numerical Reconstruction of Holograms: A New Method for Displaying Light in Flight", *Applied Optics*, Vol. 34, No. 35, pp. 8095–8099, 1995.

13. Cuche, E., P. Marquet, P. J. Magistretti and C. D. Depeursinge, "Quantitative Phase Contrast Microscopy of Living Cells by Numerical Reconstruction of Digital Holograms", *Optical Diagnostics of Living Cells II*, Vol. 3604, pp. 84 – 89, 1999.

14. Cuche, E., P. Marquet and C. Depeursinge, "Simultaneous Amplitude-contrast and Quantitative Phase-contrast Microscopy by Numerical Reconstruction of Fresnel Off-axis Holograms", *Applied Optics*, Vol. 38, No. 34, pp. 6994–7001, 1999.

15. Charrière, F., A. Marian, F. Montfort, J. Kuehn, T. Colomb, E. Cuche, P. Marquet and C. Depeursinge, "Cell Refractive Index Tomography by Digital Holographic Microscopy", *Optics Letters*, Vol. 31, No. 2, pp. 178–180, 2006.

16. Marquet, P., B. Rappaz, P. J. Magistretti, E. Cuche, Y. Emery, T. Colomb and C. Depeursinge, "Digital Holographic Microscopy: A Noninvasive Contrast Imaging Technique Allowing Quantitative Visualization of Living Cells with Subwavelength Axial Accuracy", *Optics Letters*, Vol. 30, No. 5, pp. 468–470, 2005.

17. "All Nobel Prizes in Physics", `https://www.nobelprize.org/prizes/lists/all-nobel-prizes-in-physics/`, accessed on 7 July 2022.

18. Fürhapter, S., A. Jesacher, S. Bernet and M. Ritsch-Marte, “Spiral Phase Contrast Imaging in Microscopy”, *Optics Express*, Vol. 13, No. 3, pp. 689–694, 2005.

19. Rylander, C. G., D. P. Davé, T. Akkin, T. E. Milner, K. R. Diller and A. J. Welch, “Quantitative Phase-contrast Imaging of Cells with Phase-sensitive Optical Coherence Microscopy”, *Optics Letters*, Vol. 29, No. 13, pp. 1509–1511, 2004.

20. Preza, C., D. L. Snyder and J.-A. Conchello, “Theoretical Development and Experimental Evaluation of Imaging Models for Differential-Interference-Contrast Microscopy”, *Journal of the Optical Society of America A*, Vol. 16, No. 9, pp. 2185–2199, 1999.

21. Zernike, F., “Diffraction Theory of the Knife-edge Test and Its Improved Form, the Phase-contrast Method”, *Monthly Notices of the Royal Astronomical Society*, Vol. 94, pp. 377–384, 1934.

22. Allen, R. and G. David, “The Zeiss-Nomarski Differential Interference Equipment For Transmitted-Light Microscopy”, *Zeitschrift fur Wissenschaftliche Mikroskopie und Mikroskopische Technik*, Vol. 69, No. 4, pp. 193–221, 1969.

23. Lang, W., *Nomarski Differential Interference-Contrast Microscopy*, Carl Zeiss Oberkochen, 1982.

24. Goodman, J. W., *Introduction to Fourier Optics*, McGraw-Hill, 1996.

25. Leith, E. N. and J. Upatnieks, “Reconstructed Wavefronts and Communication Theory”, *Journal of the Optical Society of America*, Vol. 52, No. 10, pp. 1123–1130, 1962.

26. Leith, E. N. and J. Upatnieks, “Wavefront Reconstruction with Diffused Illumination and Three-dimensional Objects”, *Journal of the Optical Society of America*, Vol. 54, No. 11, pp. 1295–1301, 1964.

27. Carter, W. H., "Computational Reconstruction of Scattering Objects from Holograms", *Journal of the Optical Society of America*, Vol. 60, No. 3, pp. 306–314, 1970.

28. Wolf, E. and J. R. Shewell, "Diffraction Theory of Holography", *Journal of Mathematical Physics*, Vol. 11, No. 8, pp. 2254–2267, 1970.

29. Barer, R., "Interference Microscopy and Mass Determination", *Nature*, Vol. 169, No. 4296, p. 366–367, 1952.

30. Zicha, D. and G. A. Dunn, "An Image Processing System for Cell Behaviour Studies in Subconfluent Cultures", *Journal of Microscopy*, Vol. 179, No. 1, pp. 11–21, 1995.

31. Rappaz, B., E. Cano, T. Colomb, J. Kuhn, C. D. Depeursinge, V. Simanis, P. J. Magistretti and P. P. Marquet, "Noninvasive Characterization of the Fission Yeast Cell Cycle by Monitoring Dry Mass with Digital Holographic Microscopy", *Journal of Biomedical Optics*, Vol. 14, No. 3, pp. 1 – 5, 2009.

32. Zhang, T. and I. Yamaguchi, "Three-dimensional Microscopy with Phase-shifting Digital Holography", *Optics Letters*, Vol. 23, No. 15, pp. 1221–1223, 1998.

33. Takeda, M., H. Ina and S. Kobayashi, "Fourier-transform Method of Fringe-pattern Analysis for Computer-based Topography and Interferometry", *Journal of the Optical Society of America*, Vol. 72, No. 1, pp. 156–160, 1982.

34. Cuche, E., P. Marquet and C. Depeursinge, "Aperture Apodization Using Cubic Spline Interpolation: Application in Digital Holographic Microscopy", *Optics Communications*, Vol. 182, No. 1, pp. 59–69, 2000.

35. Zhang, Y., J. Zhao, Q. Fan, W. Zhang and S. Yang, "Improving the Reconstruction Quality with Extension and Apodization of the Digital Hologram", *Applied Optics*, Vol. 48, No. 16, pp. 3070–3074, 2009.

36. Colomb, T., F. Montfort, J. Kühn, N. Aspert, E. Cuche, A. Marian, F. Charrière, S. Bourquin, P. Marquet and C. Depeursinge, "Numerical Parametric Lens for Shifting, Magnification, and Complete Aberration Compensation in Digital Holographic Microscopy", *Journal of the Optical Society of America A*, Vol. 23, No. 12, pp. 3177–3190, 2006.

37. Colomb, T., J. Kühn, F. Charrière, C. Depeursinge, P. Marquet and N. Aspert, "Total Aberrations Compensation in Digital Holographic Microscopy with a Reference Conjugated Hologram", *Optics Express*, Vol. 14, No. 10, pp. 4300–4306, 2006.

38. Kühn, J., F. Charrière, T. Colomb, E. Cuche, F. Montfort, Y. Emery, P. Marquet and C. Depeursinge, "Axial Sub-nanometer Accuracy in Digital Holographic Microscopy", *Measurement Science and Technology*, Vol. 19, No. 7, p. 074007, 2008.

39. Popescu, G., *Quantitative Phase Imaging of Cells and Tissues*, McGraw-Hill, 2011.

40. Sypek, M., "Light Propagation in the Fresnel Region. New Numerical Approach", *Optics Communications*, Vol. 116, No. 1-3, p. 43–48, 1995.

41. Axelrod, D., "Cell-substrate Contacts Illuminated by Total Internal Reflection Fluorescence", *Journal of Cell Biology*, Vol. 89, No. 1, p. 141–145, 1981.

42. Ravier, M. A., T. Tsuboi and G. A. Rutter, "Imaging A Target of ca2+ Signalling: Dense Core Granule Exocytosis Viewed by Total Internal Reflection Fluorescence Microscopy", *Methods*, Vol. 46, No. 3, p. 233–238, 2008.

43. Ellefsen, K. L., J. L. Dynes and I. Parker, "Spinning-spot Shadowless Tirf Microscopy", *PLOS ONE*, Vol. 10, No. 8, 2015.

44. Ambrose, E. J., "A Surface Contact Microscope for the Study of Cell Movements", *Nature*, Vol. 178, No. 4543, p. 1194–1194, 1956.

45. Prieve, D. C., “Measurement of Colloidal Forces with TIRM”, *Advances in Colloid and Interface Science*, Vol. 82, No. 1, pp. 93–125, 1999.

46. Pedrotti, F. L., L. M. Pedrotti and L. S. Pedrotti, *Introduction to Optics: Frank L. Pedrotti, Leno S. Pedrotti, Leno M. Pedrotti.*, Pearson Prentice Hall, 2007.

47. Ash, W. M. and M. K. Kim, “Digital Holography of Total Internal Reflection”, *Optics Express*, Vol. 16, No. 13, pp. 9811–9820, 2008.

48. Zhang, J., C. Ma, S. Dai, J. Di, Y. Li, T. Xi and J. Zhao, “Transmission and Total Internal Reflection Integrated Digital Holographic Microscopy”, *Optics Letters*, Vol. 41, No. 16, pp. 3844–3847, 2016.

49. Mandracchia, B., O. Gennari, V. Marchesano, M. Paturzo and P. Ferraro, “Label Free Imaging of Cell-substrate Contacts by Holographic Total Internal Reflection Microscopy”, *Journal of Biophotonics*, Vol. 10, No. 9, pp. 1163–1170, 2017.

50. Mandracchia, B., O. Gennari, A. Bramanti, S. Grilli and P. Ferraro, “Label-free Quantification of the Effects of Lithium Niobate Polarization on Cell Adhesion via Holographic Microscopy”, *Journal of Biophotonics*, Vol. 11, No. 8, p. e201700332, 2018.

51. Maire, G., H. Giovannini, A. Talneau, P. C. Chaumet, K. Belkebir and A. Sentenac, “Phase Imaging and Synthetic Aperture Super-resolution via Total Internal Reflection Microscopy”, *Optics Letters*, Vol. 43, No. 9, pp. 2173–2176, 2018.

52. Toy, M. F., “Wedge Prism Assisted Quantitative Phase Imaging on Standard Microscopes”, *Optics Communications*, Vol. 451, pp. 361–366, 2019.

53. Toy, M. F., C. Pache, J. Parent, J. Kühn, M. Egli and C. Depeursinge, “Dual-mode Digital Holographic and Fluorescence Microscopy for the Study of Morphological Changes in Cells Under Simulated Microgravity”, *Three-Dimensional and Multidimensional Microscopy: Image Acquisition and Processing XVII*, Vol. 7570, pp.

65 – 68, 2010.

54. Massig, J. H., "Digital Off-axis Holography with A Synthetic Aperture", *Optics Letters*, Vol. 27, No. 24, pp. 2179–2181, 2002.

55. Tippie, A. E., A. Kumar and J. R. Fienup, "High-resolution Synthetic-aperture Digital Holography with Digital Phase and Pupil Correction", *Optics Express*, Vol. 19, No. 13, pp. 12027–12038, 2011.

56. Cotte, Y., F. Toy, P. Jourdain, N. Pavillon, D. Boss, P. Magistretti, P. Marquet and C. Depeursinge, "Marker-Free Phase Nanoscopy", *Nature Photonics*, Vol. 7, No. 2, p. 113–117, 2013.

57. Choi, C. K., M. Vicente-Manzanares, J. Zareno, L. A. Whitmore, A. Mogilner and A. R. Horwitz, "Actin and α-actinin Orchestrate the Assembly and Maturation of Nascent Adhesions in A Myosin II Motor-independent Manner", *Nature Cell Biology*, Vol. 10, No. 9, p. 1039–1050, 2008.

58. Hotulainen, P. and P. Lappalainen, "Stress Fibers are Generated by Two Distinct Actin Assembly Mechanisms in Motile Cells ", *Journal of Cell Biology*, Vol. 173, No. 3, pp. 383–394, 2006.

59. Wildanger, D., J. Bückers, V. Westphal, S. W. Hell and L. Kastrup, "A STED Microscope Aligned by Design", *Optics Express*, Vol. 17, No. 18, pp. 16100–16110, 2009.

60. Guo, Z., H. Liu, L. Xiang, L. Chen, J. Yang, J. Wen, Y. Shang, T. Wang and F. Pang, "Generation of Perfect Vortex Beams with Polymer Based Phase Plate", *IEEE Photonics Technology Letters*, Vol. 32, No. 10, p. 565–568, 2020.

61. Nock, V. and R. J. Blaikie, "Fabrication of Optical Grayscale Masks for Tapered Microfluidic Devices", *Microelectronic Engineering*, Vol. 85, No. 5, pp. 1077–1082, 2008.

62. Rooman, C., M. Kuijk, R. A. Vounckx and P. L. Heremans, “Reflective-Refractive Microlens for Efficient Light-Emitting-Diode-to-Fiber Coupling”, *Optical Engineering*, Vol. 44, No. 9, pp. 1 – 5, 2005.

63. Levy, U., B. Desiatov, I. Goykhman, T. Nachmias, A. Ohayon and S. E. Meltzer, “Design, Fabrication, and Characterization of Circular Dammann Gratings Based on Grayscale Lithography”, *Optics Letters*, Vol. 35, No. 6, pp. 880–882, 2010.

64. Losurdo, M., M. Bergmair, G. Bruno, D. Cattelan, C. Cobet, A. de Martino, K. Fleischer, Z. Dohcevic-Mitrovic, N. Esser, M. Galliet and et al., “Spectroscopic Ellipsometry and Polarimetry for Materials and Systems Analysis at the Nanometer Scale: State-of-the-art, Potential, and Perspectives”, *Journal of Nanoparticle Research*, Vol. 11, No. 7, p. 1521–1554, 2009.

65. Hall, R. L., “Phase sensitive optical monitor for thin film deposition”, U.S. Patent 4906844, March 6,1990.

66. Rebey, A., T. Boufaden and B. El Jani, “In-situ Optical Monitoring of the Decomposition of GaN Thin Films”, *Journal of Crystal Growth*, Vol. 203, No. 1, pp. 12–17, 1999.

67. Minami, K., H. Tosaka and M. Esashi, “Optical In-situ Monitoring of Silicon Diaphragm Thickness During Wet Etching”, *Proceedings IEEE Micro Electro Mechanical Systems An Investigation of Micro Structures, Sensors, Actuators, Machines and Robotic Systems*, pp. 217–222, 1994.

68. Mackus, A. J. M., S. B. S. Heil, E. Langereis, H. C. M. Knoops, M. C. M. van de Sanden and W. M. M. Kessels, “Optical Emission Spectroscopy as A Tool for Studying, Optimizing, and Monitoring Plasma-assisted Atomic Layer Deposition Processes”, *Journal of Vacuum Science & Technology A*, Vol. 28, No. 1, pp. 77–87, 2010.

69. Gureyev, T. E., A. Roberts and K. A. Nugent, “Phase Retrieval With the

Transport-of-Intensity Equation: Matrix Solution With Use of Zernike Polynomials", *Journal of the Optical Society of America A*, Vol. 12, No. 9, pp. 1932–1941, 1995.

70. Bhaduri, B., C. Edwards, H. Pham, R. Zhou, T. H. Nguyen, L. L. Goddard and G. Popescu, "Diffraction Phase Microscopy: Principles and Applications in Materials and Life Sciences", *Advances in Optics and Photonics*, Vol. 6, No. 1, pp. 57–119, 2014.

71. Edwards, C., A. Arbabi, G. Popescu and L. L. Goddard, "Optically Monitoring and Controlling Nanoscale Topography During Semiconductor Etching", *Light: Science & Applications*, Vol. 1, No. 9, 2012.

72. Takajo, H. and T. Takahashi, "Noniterative Method for Obtaining the Exact Solution for the Normal Equation in Least-squares Phase Estimation from the Phase Difference", *Journal of the Optical Society of America A*, Vol. 5, No. 11, pp. 1818–1827, 1988.

73. Harm, W., S. Bernet, M. Ritsch-Marte, I. Harder and N. Lindlein, "Adjustable Diffractive Spiral Phase Plates", *Optics Express*, Vol. 23, No. 1, pp. 413–421, 2015.

APPENDIX A: PHASE AND AMPLITUDE IMAGES FOR MICROSPHERES

The phase and amplitude images obtained from 380 nm microspheres are shown in Figure A.1. The Figure A.1a shows the bright field image of a microsphere couple, Figure A.1b and c shows the profile obtained from combined phase and amplitude images, respectively. Figure A.1d and e show phase images obtained from single sided illumination, and the lateral vector belonging to illumination is given by the red arrow. Figure A.1g and h show amplitude images obtained from single sided illumination, and again the lateral vector belonging to illumination is given by the red arrow. Figure A.1f and i show the combined phase and amplitude images, respectively.

The effect of synthetic aperture and illumination direction can be seen more clearly in the closeup phase, and amplitude images belong to this FoV as shown in Figure A.2. Figure A.2a,h and o shows bright field images of microsphere pairs. Figure A.2b,c,i,j,p and q shows phase images obtained by illumination from single direction. Similarly Figure A.2e,f,l,m,s and t shows amplitude images obtained by illumination from single direction. Figure A.2d,k and r shows combined phase images. Figure A.2g,n and u shows combined amplitude images.

The phase and amplitude images obtained from 300 nm microspheres are shown in Figure A.3. The Figure A.3a shows the bright field image of a microsphere couple, Figure A.3b and c shows the profile obtained from combined phase and amplitude images, respectively. Figure A.3d and e show phase images obtained from single sided illumination, and the lateral vector belonging to illumination is given by the red arrow. Figure A.3g and h show amplitude images obtained from single sided illumination, and again the lateral vector belonging to illumination is given by the red arrow. Figure A.3f and i show the combined phase and amplitude images, respectively.

Closeup phase, and amplitude images for 300 nm microspheres are shown in Figure A.4. Figure A.4a,h and o shows bright field images of microsphere pairs. Figure A.4b,c,i,j,p and q shows phase images obtained by illumination from single direction. Similarly Figure A.4e,f,l,m,s and t shows amplitude images obtained by illumination from single direction. Figure A.4d,k and r shows combined phase images. Figure A.4g,n and u shows combined amplitude images.

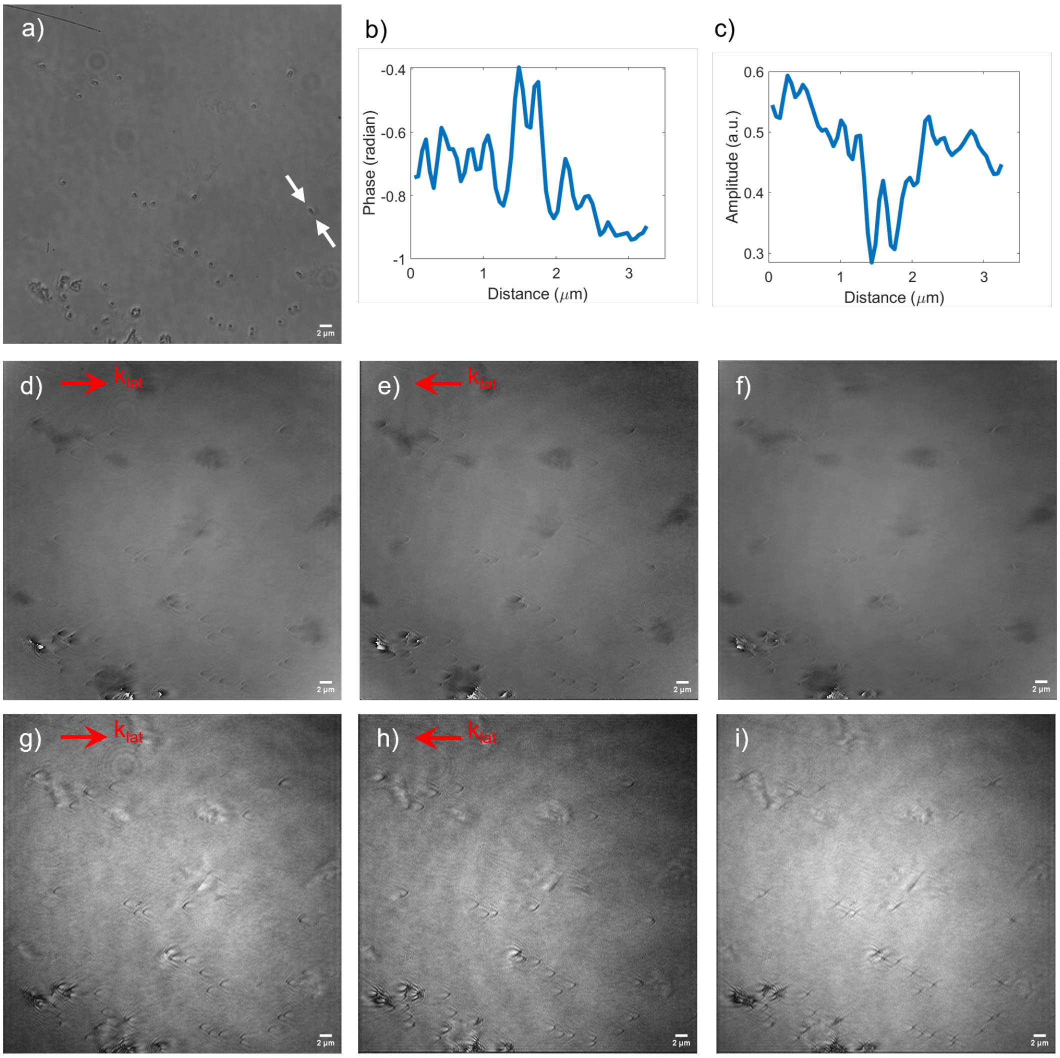

Figure A.1. Obtained bright-field, phase and amplitude images for 380 nm diameter microspheres.

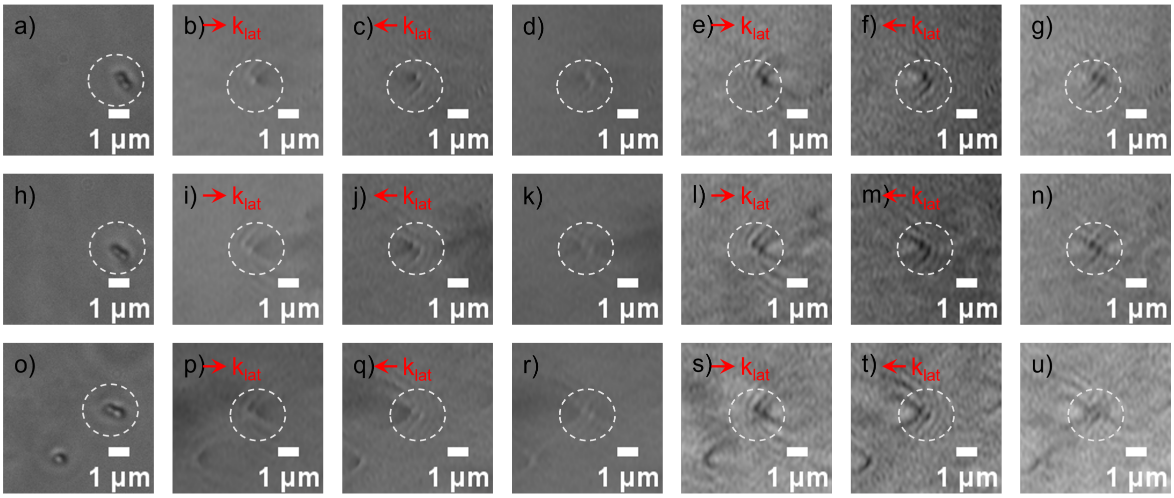

Figure A.2. Closeup of obtained bright-field, phase and amplitude images for 380 nm diameter microspheres.

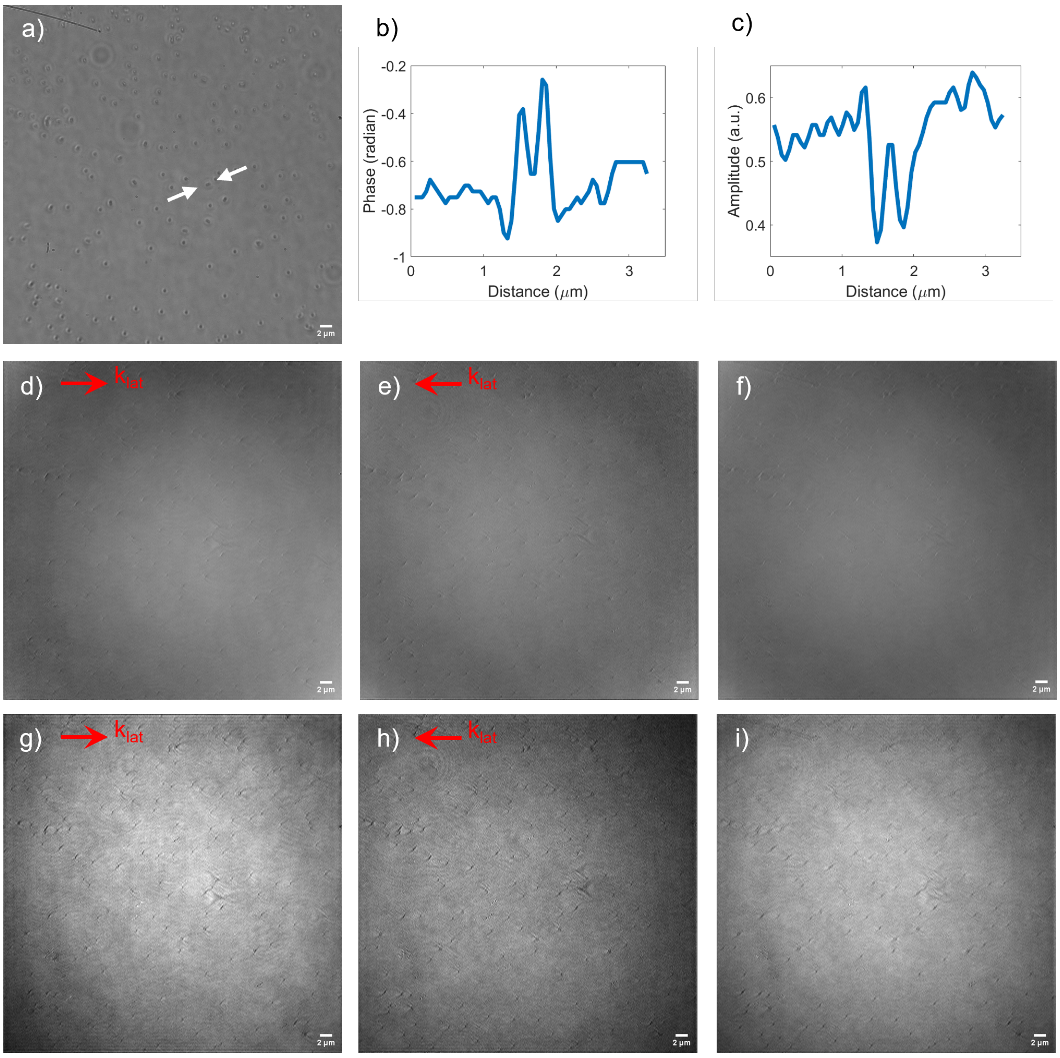

Figure A.3. Obtained bright-field, phase and amplitude images for 300 nm diameter microspheres.

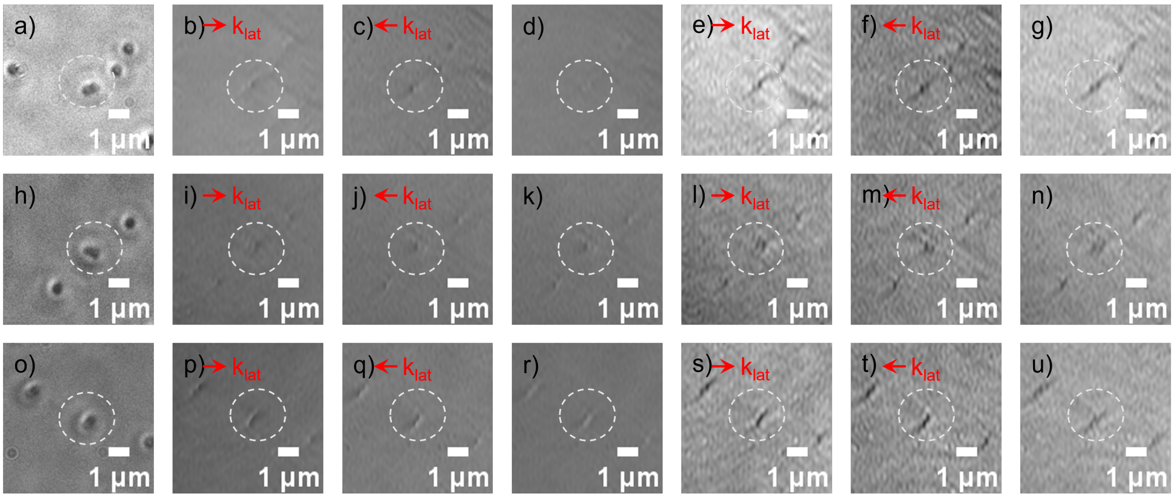

Figure A.4. Closeup of obtained bright-field, phase and amplitude images for 300 nm diameter microspheres.